CHALMERS
UNIVERSITY OF TECHNOLOGY

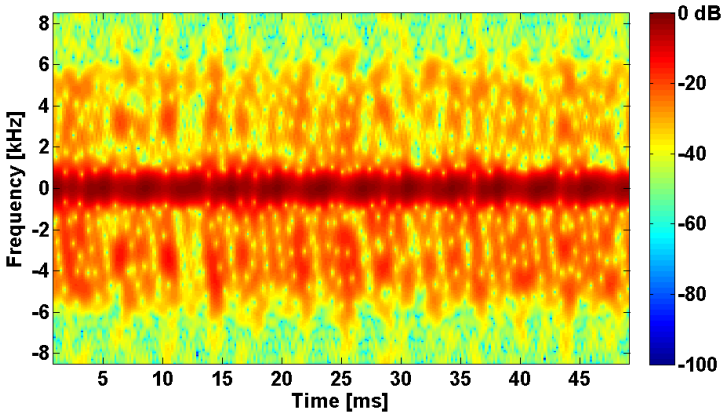

Modeling multicopter radar return

A study in discrimination of multicopter UAVs from birds using the micro-Doppler effect

Master's thesis in Applied Physics

BJÖRN KARLSSON

Department of Electrical Engineering
CHALMERS UNIVERSITY OF TECHNOLOGY
Gothenburg, Sweden 2017

Master's thesis 2017

Modeling Multicopter Radar Return

A Study in Discrimination of Multicopter UAVs from Birds Using the Micro-Doppler Effect

BJÖRN KARLSSON

CHALMERS
UNIVERSITY OF TECHNOLOGY

Department of Electrical Engineering
Division of Signal processing and Biomedical engineering
Chalmers University of Technology
Gothenburg, Sweden 2017

Modeling Multicopter Radar Return
A Study in Discrimination of Multicopter UAVs from Birds Using the Micro-Doppler Effect
BJÖRN KARLSSON

Supervisors: Patrik Dammert, Saab Surveillance
Björn Engström, Saab Surveillance
Examiner: Thomas Rylander, Electrical Engineering

Master's Thesis 2017
Department of Electrical Engineering
Division of Signal processing and Biomedical engineering
Chalmers University of Technology
SE-412 96 Gothenburg
Telephone +46 31 772 1000

Cover: Left: simulated micro-Doppler signature at X-band of a hexacopter. Right: hexacopter in flight. From [1]. CC-BY-SA.

Gothenburg, Sweden 2017

Modeling Multicopter Radar Return
A Study in Discrimination of Multicopter UAVs from Birds Using the Micro-Doppler Effect
BJÖRN KARLSSON
Department of Electrical Engineering
Chalmers University of Technology

ABSTRACT

There is an emerging need for detection of multicopter unmanned aerial vehicles (UAVs) and a radar solution is considered for this. However, multicopters and birds have very similar radar cross-sections thus a radar application is not easily realised. Although, the fast moving propellers of the multicopter suggests that, using the micro-Doppler effect, a distinction between the two can be made. This thesis investigates the expected radar return of different multicopter UAVs through simulation techniques and how a monostatic, pulsed Doppler radar may be designed to discriminate them from birds.

The part of the multicopter which contributes the most to its micro-Doppler signature is the propeller. Therefore, calculations of the radar return are focused on the propellers. The static radar return is calculated in the simulation software Ansys HFSS using a 3D model of a propeller. In this simulated environment, different scenarios are created where properties such as polarisation, dielectric constant, length, carrier frequency and angle of illumination are varied and the effect of using ducted propellers is studied. The studied radar bands are L-, S-, C- and X-band. The results of these calculations are then compared to suggested mathematical models that predict the radar cross-section of propellers and very good agreement is observed. Thereafter, the dynamic radar return is simulated, where inverse synthetic aperture radar (ISAR) imaging techniques are tested and micro-Doppler signatures are generated. A simple technique to extract discriminative features from the micro-Doppler signature based on singular value decomposition (SVD) is also analysed and it can reveal both spectrum width and periodicity. Based on the simulations, the impact of different radar design parameters such as the pulse repetition frequency (PRF), illumination time, carrier frequency and polarisation on the detection of multicopters is investigated and conclusions are drawn on how these parameters are chosen for optimal detection.

Keywords: UAV, multicopter, birds, micro-Doppler effect, radar, simulation

ACKNOWLEDGEMENTS

First of all, I would like to thank my supervisors at Saab Surveillance, Patrik Dammert and Björn Engström, for our many interesting discussions and for your encouragement and guidance throughout this project. Also, I thank my supervisor and examiner at Chalmers University of Technology, Thomas Rylander, for our in-depth, theoretical discussions about radar and electromagnetic computations in general.

Lastly, a big thank you to employees at Saab for taking time for me whenever I had questions and also for making me feel welcome with kindness and by inviting me to activities such as "fika-Fridays". Also, warmest of thanks to my fellow Master's thesis students at Saab for your great ideas and support during this project, and for greatly contributing to the overall joyful experience of these past months.

Björn Karlsson, Gothenburg, August 2017

CONTENTS

LIST OF FIGURES

LIST OF TABLES

LIST OF ABBREVIATIONS

CAD – Computer aided design

CCW – Counter-clockwise

CW – Clockwise

FEM – Finite element method

ICA – Independent component analysis

IFFT – Inverse fast Fourier transform

IFT – Inverse Fourier transform

ISAR – Inverse synthetic aperture radar

PCA – Principal component analysis

PEC – Perfect electric conductor

PML – Perfectly matched layer

PRF – Pulse repetition frequency

PRI – Pulse repetition interval

RCS – Radar cross-section

RPM – Revolutions per minute

STFT – Short time Fourier transform

SVD – Singular value decomposition

UAV – Unmanned aerial vehicle

1 INTRODUCTION

In this chapter, the problem being studied in this thesis is defined. The background as to why the study has been conducted is first given, followed by a description of what the aim of the study is and how the scope is set. A brief summary of what has previously been done in the research field is given to put the contribution of this study in perspective to current theoretical knowledge.

1.1 Demand for detection of multicopters

It is noticeable that over recent years, the popularity of small multirotor unmanned aerial vehicles (UAVs), or multicopters, has reached new heights and the market for small UAVs is also predicted to increase over coming years [2]. The multicopter is a rather complex structure and it is not an easy task to stabilise this aerial vehicle as there needs to be good communication between the individual rotors with good control models. However, technical advancements within the field have made this technology cheaper and available to the general public and multicopters can nowadays be bought as ready-to-fly models or built in a more customised manner from manufactured modules. The complete vehicle is also not too difficult to use and civilians can therefore use multicopters for leisure activities such as aerial photography or drone racing. Other potential applications with a more professional approach that can be seen for these UAVs are to use them in farming, monitoring wildlife or industrial logistics [2].

This increased availability of the technology to the public has also introduced a number of complications. As multicopters are easily obtained they may be used by people to perform illegal activities or to disturb order and as a result, legislation is being made in countries around the world to regulate dangerous activities [3]. Possible uses could be to disrupt air traffic at airports, smuggle goods into prisons or deploy poisonous biological or chemical substances in crowded areas such as big events. Additionally, a usually long operating distance makes it necessary to detect the UAV in the air and on a long enough distance to be able to react with countermeasures. Therefore, in order to be better prepared against these activities, a demand for good detection of multicopters has arisen and one way to realise detection and classification is through the use of a radar solution.

However, it is not an easy task to utilise radar for this purpose. Multicopters are typically of small sizes and their electromagnetic response is in amplitude comparable to that of birds. Thus, lowering the detection thresholds of a radar system in order to find these smaller targets leads most likely to many, unwanted detections from nearby birds and as a result of this, the system may become saturated. However, one way of discriminating multicopters from birds may be to use the micro-Doppler effect which describes the internal motion pattern of the target, which gives it a distinct and unique signature. To be able to use the radar as a means of detection of multicopters, it is necessary that the target classification is fast and robust and, thus, the different design parameters of the radar system need to be optimised for the target of interest. This report investigates what radar returns (i.e. the signal received at the radar after it has scattered from a target) may be expected from multicopters and birds and how classification is affected by radar design parameters.

1.2 Objective

The aim of this study is to use simulation techniques to investigate the radar return of multicopters for different radar waveforms and for different multicopter models, and how the radar return then can be used to detect small multicopters using a monostatic, pulsed Doppler radar.

To achieve the aim, the work is focused on the following aspects:

- Simulate the radar cross-section of different types of multicopters using two simulation tools Matlab and HFSS with appropriate numerical models such as the point scatter model and finite element method.
- Calculate and analyse the micro-Doppler signature generated by the simulated radar returns and suggest ways to detect multicopters and distinguish them from nearby clutter or nuisance objects such as birds.
- Analyse how radar design parameters such as carrier frequency, pulse repetition frequency and illumination time affect detection for different targets and distances.

1.2.1 Scope

The focus of this study lies on the detection of multicopters from the electromagnetic response that they give. Therefore, hardware structure of the radar system is not part of the scope of this thesis and it is assumed that a certain investigated waveform can be generated. However, relevant waveforms that are commonly used in radar applications receive focus in order to optimise parameters that affect detection.

There are many types of radars that can be used, but in this study only the monostatic, pulsed Doppler radar is considered. Other types, such as bistatic-/multistatic radars or continuous wave radar are not part of the thesis.

The conditions are assumed to be perfect in the simulated environment, i.e. clutter other than birds is not considered. The effect of missing data points is also not considered.

The type of target that is detected is limited to small multicopter UAVs that are available easily to the public. Even though larger multicopters are not investigated in this project, they most likely have a similar behaviour as smaller ones. This relation is however not thoroughly investigated or considered.

1.3 Previous work

The increased demand for fast and robust radar detection of multicopters has led to many research groups investigating the area. As a result of this, rather recent publications that show good results can be found on the subject.

There have been several studies of the radar cross-section (RCS) and micro-Doppler signature of birds. In [4], a vertically polarised X-band Synthetic Aperture Radar (SAR) is used for detection of gannets and it is concluded that extracted micro-Doppler spectrograms vary greatly depending on aspect angle and is best observed at head-on, even though RCS of birds is larger at broadside than on head-on/tail-on incidence [5]. This was believed to be due to the

low RCS of the wings, thus generating hardly noticeable Doppler shifts in comparison to the body. It has been seen that the polarisation has an effect on the detection of birds, where horizontal polarisation yields 2.5 times greater reflectivity than vertical polarisation when migrating birds are illuminated at broadside [6].

Studies have shown that discrimination of multicopters and birds can be achieved in a robust way. A classification rate of 92% using a singular value decomposition (SVD) classification method in combination with machine learning has been reported, although tested at a short distance to target of less than 30 m [7]. The discrimination of multicopters from birds has also been thoroughly examined by Torvik, where the focus is on detection at radar frequency bands L- and S-band [8].

The radar return of multicopters has been investigated theoretically and experimentally, where the experiments have involved measurements in field tests as well as in anechoic chamber [9, 10, 11, 12]. There have been a few studies on the properties of the propellers and their impact on the radar return, where a limited selection of propellers were investigated [11, 13]. A commercial, low-cost radar that is able to detect multicopters has been developed by the company QinetiQ based on one of these studies [11]. An initial study has also been conducted at Saab Surveillance, where the radar return is numerically calculated for a propeller and it is compared to thin cylinder models [14].

Although it has been shown that a working radar system can be developed, there are few publications that show extensive research on how the radar return varies for different models of multicopter UAV depending on target properties such as size, shape, material etc. The PhD thesis in [8] is extensive, although mainly focusing on two frequency bands. The dependence of radar return on these properties is important knowledge for designing a radar system with optimised radar design parameters for the specific target discrimination.

1.4 Report outline

Chapter 2 describes the theoretical background of the project as well as the terminology used throughout this report. This includes details about the target of interest, the multicopter, and the radar system with its associated phenomena. An explanation of the models used in the electromagnetic simulations and their approximations are given here as well. In Chapter 3, the simulation software used and the relevant parameters that can be changed are described first. Details about the static electromagnetic response of a single propeller are thereafter presented, where the impact of the variation of parameters such as material and carrier frequency is investigated. The propeller is subsequently analysed dynamically in Chapter 4, where a full multicopter is modeled based on the single propeller model. A simple method of extracting discriminative features from the radar return is also studied in this chapter and a comparison with the expected radar return of birds is given. Finally, the results from the calculations are presented and compared in an analysis of radar design parameters and discussed from a broader perspective in Chapter 5 and a summary of the conclusions of the study is given in Chapter 6.

2 MULTICOPTER STRUCTURE AND RADAR THEORY

In order to be able to detect a certain target, a clear understanding of the characteristics of the target is necessary. Therefore, the multicopter is first described in terms of its typical size, structure and behaviour. The structure and properties of the propellers are also discussed in a detailed way as they have a significant impact on the radar return and thus can be used as a classification feature.

Aside from information about the target, it is also important to have knowledge about the radar waveform being used for detection and what kind of information that can be extracted from its echo from the target. As the simulated radar system is a monostatic, pulsed Doppler radar, this type of radar is further described along with different phenomena and radar terminology such as the radar cross-section and micro-Doppler effect associated with this kind of radar. The simulation of radar returns is a central part of this study, thus numerical simulation models for calculating radar returns and the approximations being made when they are used are also discussed.

2.1 Multicopter structure and function

A multicopter is a multirotor aerial vehicle that uses the lift force of rotating propellers to gain or maintain height in the air. Unlike the helicopter that uses one propeller mainly for lift force and steering, and one propeller for eliminating torque, the multicopter uses multiple propellers that each is used for generating lift force and to steer the vehicle.

The multicopter can be designed in many different ways. They may have different number of propellers, varying from the three propeller tricopter to the eight propeller octocopter. The body of the multicopters can be structured differently as well with different added features. Such features include a protective frame or duct around the propellers, landing gear, camera equipment etc. Each part of the multicopter may also be of very different materials such as plastics, glass reinforced plastics, carbon fibre or metals. Three examples of typical multicopter design for commercial models are shown in Fig. 2-1, where two quadcopters and one hexacopter are shown with their different individual features. Multicopters can therefore be very different from each other in terms of size, shape, structure and material and this makes it difficult to characterise and detect them using radar techniques.

a) **b)** **c)**

Fig. 2-1 Three examples of commercial multicopter models: **a)** Parrot AR Drone 2.0; **b)** DJI Phantom 2 Vision+; and **c)** Yuneec Typhoon H. Features such as camera equipment, landing gear and protective frame can be added to many models. From [15, 16, 17]. CC-BY-SA.

2.1.1 Structural properties

A common denominator of all multicopters is the use of rotating propellers that can vary greatly in shape, size and materials. In addition, the propellers can also be arranged in a number of ways with different benefits and drawbacks.

A very common multicopter is the quadcopter with four propellers. In quadcopters, the propellers can mainly be arranged in three different ways: X4-, H4- or +4-configuration. Here, the X4-configuration is the most common as it allows for a better camera placement without obstruction of the vehicle frame in the forward direction. The three configurations of the propellers of a quadcopter are illustrated in Fig. 2-2. Two of the rotors are rotating clockwise (CW) and two rotors are rotating counter-clockwise (CCW) as the quadcopter is viewed from above. This yields a zero net torque generated from the spinning propellers, which makes the vehicle keep its orientation during hover.

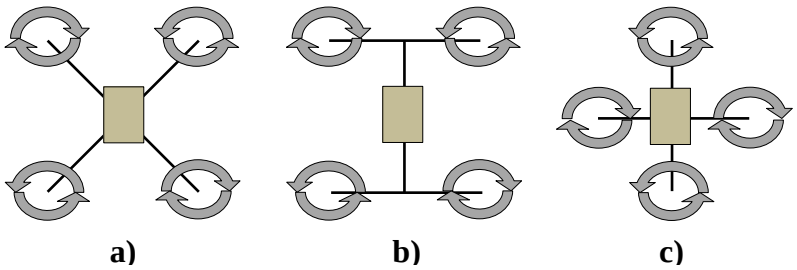

Fig. 2-2. Propeller configurations for quadcopters: **a)** X4-configuration; **b)** H4-configuration; and **c)** +4-configuration. Each pair of opposite propellers rotate in the same direction, i.e. clockwise or counter-clockwise.

Other common multicopters are the hexacopter with six propellers and the octocopter with eight propellers. The propeller configurations are typically structured as equally spaced out propellers at a fixed distance from the vehicle body with alternating CW and CCW rotation. Less common configurations are the Y6 and X8 configurations. These configurations use three and four pairs of propellers, respectively, where each pair consists of one CW rotating and one CCW rotating propeller on top of each other. This is much like the tricopter (or Y3-configuration) with three propellers, which is popular when making lightweight multicopters, and the X4 quadcopter. However, the increased number of propellers allows for a larger payload to be carried by the vehicle at the cost of a lower motor efficiency. The reduced efficiency is due to the fact that the added propeller is rotating in much more turbulent air.

The size of the multicopter may vary quite largely. The larger multicopters, often intended for aerial photography or carrying different kinds of equipment, are of sizes around 1000-1500 mm in wingspan, when measured diagonally across the vehicle and including the propellers. The smallest models available can fit in one's hand. Commercial quadcopters for leisure activities are typically in the range of 250-1000 mm in measured wingspan. The material of the body is of a lightweight and durable material, which is usually plastic or carbon fibre.

Some models may have protective frames or ducts around the propellers. These can either be in the form of a covering cylinder or duct as shown for the multicopter in Fig. 2-1a) or as a frame mounted underneath the propeller that is stretching out beyond the propeller diameter. A study has shown that propellers in ducts yield almost the same flight performance as non-ducted propellers but the use of ducts also introduces a decrease in endurance of the vehicle [18]. Protective frames of this type may be of different types of lightweight materials such as carbon fibre or plastics and frames designed for indoor usage may consist of plastic foams such as Styrofoam.

2.1.2 Propeller structure

The propeller of the multicopter is an especially interesting part as it is a common denominator of all multirotor aircraft. The standard for describing its geometric properties is to provide the diameter and the pitch in inches, e.g. 3x4.5” or 3045 would mean a 3” diameter and a 4.5” pitch. The diameter is the diameter of the circle that the propeller creates as it spins about its centre and it is effectively the length of the propeller. The pitch is the distance along the propeller axis that the propeller moves in one revolution, should it rotate in a soft solid, like e.g. a screw in wood. Thus, it is a measure of how aggressive the propeller is as it is rotating in the air and is also an indication of its shape, a higher pitch results in a faster multicopter given a fixed number of revolutions per minute (RPM) at the expense of using more power. Propellers come in all sizes and shapes. However, typical geometrical properties for normal or large sized multicopters vary from about 5” to 20” in diameter and about 3” to 7” in pitch. A propeller can also consist of more than two blades, which is the most common arrangement. Three blades are rather common for multicopters, whereas four or more are not used widely. Adding an extra blade introduces more lift force and uses more power as the added extra blade needs to cut through the air.

The propeller has a curved shape to generate the lift force and each blade of the propeller is at an angle such that the upper edge with a larger radius of curvature is facing in the rotational direction. This means that CW and CCW propellers are mirrored with respect to each other. The radius of curvature is greatest near the centre hub and is gradually decreasing towards the tips. For aerodynamic reasons, a larger radius of curvature generates equal lift as comparable to points located closer to the tip of the propeller, which have a smaller radius of curvature but move faster than points near the centre. Thus the shape of the blade varies to achieve equal lift force for all points along the propeller.

The material of the propeller needs to be stiff and durable while preferably also being lightweight. The most common alternatives to achieve these specifications are plastics, such as ABS or nylon, and composite materials, such as carbon fibre. However, materials can vary quite largely from lightweight metals to glass fibre reinforced plastics or even wood.

2.1.3 Characteristic behaviour

Multicopter UAVs are difficult to detect with radar systems. They fall under the LSS category of radar targets which stands for low, slow and small as UAVs in this category typically fly on a low altitude, move slowly and have a small RCS. The small RCS is related to their small physical size. Using the NATO classification guide, that was established on the JCGUAV

meeting in September 2009 [19], commercial multicopters fall into the Class I Micro and Class I Mini categories which include UAVs weighing less than 2 kg and 20 kg, respectively.

Although the translational speed of the vehicle body is relatively slow, the rotational speed of the individual propellers is typically very fast. The rotational rate of a propeller can exceed 10000 RPM which, using the relation

$$v_{tip} = \omega r = 2\pi \cdot RPS \cdot r = 2\pi \frac{RPM}{60} r = \frac{\pi}{30} \cdot RPM \cdot r \tag{2.1}$$

where r is half the diameter of the propeller, corresponds to a propeller tip speed of v_{tip}=133 m/s for a propeller diameter of 10". Tip speed is limited by the pitch and diameter of the propeller and the motors, and it also depends on the momentary acceleration. It is also not exceeding the speed of sound as it would cause too much strain on the material. It can however be assumed to be around 100 m/s (or around 7500 RPM) on average while hovering. A smaller propeller also generally needs to rotate faster than a larger one in order to generate enough lift force. Thus, the RPM is typically slightly decreasing with increased propeller diameter for hover operation. The rotor and its rapid rotation influences the RCS with a clearly defined periodicity over small time intervals. This is a characteristic of multicopters that is much different from birds which have a wing beat frequency of 0-20 Hz [20], which yields much slower variations in the RCS or even no beat frequency as birds may glide at times.

As a multicopter starts accelerating, it tilts the body in the direction it is headed, which allows the thrust of the propellers to generate forward motion. This tilt can be quite large and a tilt angle of about 40° is plausible, which could reveal propellers that are otherwise hidden by the vehicle body or ducts.

2.2 Pulsed Doppler radar working principle

A well-known physical phenomenon within the field of wave theory is the Doppler effect. It states that a moving source of an emitted wave changes the frequency of the emitted signal when it is perceived by an external observer. If the source moves towards the observer (or, equivalently, the observer moves towards the source), the frequency of the perceived signal is shifted to a higher frequency than the emitted signal and if the source moves away from the observer, the frequency is shifted to a lower frequency than the emitted signal. The magnitude of the frequency shift is called the Doppler shift and it is positive for approaching targets and negative for receding targets. This phenomenon can commonly be observed in for example that the sound of an approaching ambulance siren has a higher pitch whereas an ambulance siren that moves away from the observer has a lower pitch.

In radar applications, the Doppler effect can be used to acquire velocity information about a target by analysing the frequency content of a received wave and when using a pulsed Doppler radar, one gets information about the distance as well as the velocity. This is achieved by sending short pulses of microwave waveforms and, as they reflect against the target and are received at the radar, the time difference gives the distance and the Doppler shift gives the radial velocity. The radial velocity is measured along the radar line of sight.

Thus, if a target is moving strictly perpendicular to the line of sight of the radar it does not yield any Doppler shift. If we assume that the target's velocity v is much smaller than the speed of light, i.e. $v \ll c$, we can neglect any relativistic effects and the Doppler shift measured by a monostatic Doppler radar is then given by

$$f_D = 2v\frac{f_t}{c} = \frac{2v}{\lambda}, \tag{2.2}$$

where f_t is the transmitted frequency and λ is the transmitted wavelength.

An important design parameter of the pulsed Doppler radar is the pulse repetition frequency (PRF), which is the frequency at which the pulses are sent out from the radar system. The PRF influences the distance and velocity measurements. The maximum radial velocity is dependent on the maximum Doppler shift, which depends on the sampling frequency. Given the Nyquist sampling theorem from signal theory, the sampling frequency needs to be twice the maximum frequency content of the measured signal to avoid aliasing. The sampling frequency of a Doppler radar is the PRF. Thus, (2.2) with the Nyquist criterion gives us the maximum velocity

$$v_{max} = \frac{cf_{D,max}}{2f_t} = \frac{c \cdot PRF}{4f_t} = \frac{\lambda \cdot PRF}{4}. \tag{2.3}$$

The maximum distance on the other hand is given by the time it takes for a radiated wave to travel the distance to the target and back to the radar system before another wave has been emitted. This is expressed as

$$r_{max} = \frac{1}{2}\Delta tc = \frac{c}{2 \cdot PRF}, \tag{2.4}$$

where Δt is the time between pulses, also called the pulse repetition interval (PRI). From (2.3) and (2.4) it is concluded that there must be a trade-off between maximum distance and velocity when choosing the PRF for the radar system and this is known as the Doppler dilemma. The Doppler dilemma can be expressed as a multiplication of the maximum velocity with the maximum distance, which becomes

$$v_{max}r_{max} = \frac{\lambda \cdot PRF}{4}\frac{c}{2 \cdot PRF} = \frac{\lambda c}{8}. \tag{2.5}$$

It is seen in (2.5) that the product is a constant which is only dependent on the transmitted wavelength of the radar system and is independent of the PRF. Thus, an increase in the maximum velocity results in a decrease in the maximum distance and vice versa.

The waveform used in pulsed Doppler radars is apart from the PRF also characterised by the carrier frequency, pulse width, bandwidth, polarisation and illumination time. The carrier frequency is the frequency used by the radar system and it is, for radar search and track applications, commonly in the range from about 1 GHz to 12 GHz [21]. This frequency range is divided into four different radar bands, which are listed in Tab. 2-1 with their respective frequency ranges. The pulse width is the length of one emitted pulse in time and is

approximately 1-100 μs. The bandwidth is the added frequency content (in addition to the carrier frequency) that emerges from that the emitted pulse has a finite width. The frequency content of the signal forms a spectrum in the frequency domain, centred on the carrier frequency and the bandwidth is the width of this spectrum and it is in the order of 100 MHz for radar systems. The emitted wave also has a polarisation which can be horizontal, vertical, linear or circular. The polarisation may be chosen for easier detection of the target. When a radar system is designed to emit and receive horizontally polarised waves, it is called HH-polarisation and, for vertically polarised waves, it is called VV-polarisation. The illumination time, also called integration time, of a target is the time that the radar main radiating lobe is illuminating the target.

Tab. 2-1. Frequency bands commonly used in search and track radar and their respective operating frequency ranges.

Frequency band	L-band	S-band	C-band	X-band
Frequency range	1-2 GHz	2-4 GHz	4-8 GHz	8-12 GHz

2.3 Radar return

When designing a radar system for detection of a certain target, it is important to know the target's response to electromagnetic radiation. This response is called the radar return and it is characterised mainly by the RCS of the target. However, when using a Doppler radar, as is investigated in this study, additional information can be extracted from the target's generated frequency spectrum that arises from the micro-Doppler effect.

2.3.1 Radar cross-section

The RCS of an object describes how much of incoming radiation that is reflected back towards the observer. This is for most objects highly dependent on the angle of incidence since a complex structure may reflect differently in different directions and wave phenomena such as creeping waves or scattering from sharp edges can affect the RCS greatly. The RCS is most often described in a diagram in polar coordinates and it shows the dependence of the RCS on the azimuth angle φ for a fixed elevation angle θ in a spherical coordinate system, which is shown in Fig. 2-3a). An example of the HH-polarisation of the RCS is shown in Fig. 2-3b) for a perfectly conducting cylinder of radius r=5 mm and length L=200 mm. Here, the frequency is 10 GHz and θ=90°. It is clear that the RCS varies rapidly with the azimuth angle φ.

The RCS is often denoted σ and is defined [22] as

$$\sigma = \lim_{R\to\infty} 4\pi R^2 \frac{\left|\overrightarrow{E_s}\right|^2}{\left|\overrightarrow{E_i}\right|^2}, \tag{2.6}$$

where R is the distance from the scatterer to the field point where the scattered field $\overrightarrow{E_s}$ is calculated. Here, $\overrightarrow{E_i}$ is the incident electric field of a plane wave. The scattered electric field depends on the frequency of the incident wave, or, expressed differently, the relation of the

wavelength in comparison to the size of the scattering object and other length scales that describes its geometry. If such a length scale a is much larger than the wavelength, $\lambda \ll a$, then it is within the *optical region* and the RCS is independent of the frequency for some simple scatterers such as the metal sphere. The frequency dependence of the RCS in this region may be much more complicated for more complicated geometries or dielectric scatterers. When $\lambda \gg a$, it is within the *Rayleigh Region* and the RCS is rapidly decreasing with increased wavelength. Lastly, when the length scale a is comparable to the wavelength, $\lambda \approx a$, it is within the *Mie Region* and the RCS has in general a rather complicated dependence with respect to frequency.

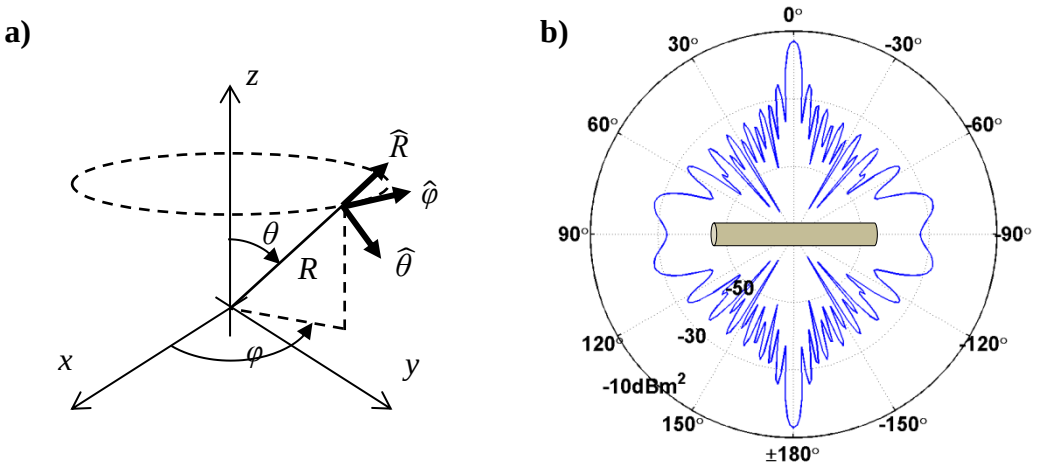

Fig. 2-3. **a)** Spherical coordinate system definition with unit vectors $\hat{R}$, $\hat{\theta}$ and $\hat{\varphi}$, and values: distance R, elevation θ and azimuth φ. **b)** RCS of a perfectly conducting cylinder, oriented along the y-axis with radius r=5mm and length L=200 mm, given in polar coordinates for different azimuth angles -180°<φ<180° and for elevation angle θ=90°. The radar waveform uses HH-polarisation and a frequency f=10 GHz.

For dielectric scatterers, the radar return is also affected by the dielectric permittivity ε of the material, which can be expressed as a complex number

$$\varepsilon = \varepsilon' - j\varepsilon''. \tag{2.7}$$

Here, the real part ε' describes the medium's ability to store electric energy and the imaginary part ε'' is related to the losses in the medium. Both the real and imaginary part of the permittivity may depend on the frequency and it can be very complicated, which requires accurate measurements for each individual material and frequency to be considered. For example, water is very transparent to visible light but is highly opaque at both higher and lower frequencies in the electromagnetic spectrum. One way to describe power losses in a medium is to use the loss tangent $\tan\delta$. The loss tangent is given by

$$\tan\delta = \frac{\varepsilon''}{\varepsilon'} \tag{2.8}$$

and gives the ratio between ε'' and ε'.

The half-power lobe width is the sector of opening angle $\Delta\varphi$ in radians where the RCS is above half (-3 dB) of its maximum value. A suggested model to approximate the lobe width of a small propeller illuminated around broadside is

$$\Delta\varphi \cong \frac{\lambda}{2L}, \tag{2.9}$$

where L is the total length or diameter of the propeller. This model is in contrast to the expression found in [23] where the lobe width is approximated as $\Delta\varphi=\lambda/(L/2)$ for a helicopter rotor blade, where L is the diameter. Another approximation is to use the broadside lobe width of a thin, circular cylinder with a radius r much smaller than its length L, i.e. $r \ll L$. An expression for the RCS of a thin cylinder near broadside is developed in [24] and based on that expression, a broadside lobe width of approximately $\Delta\varphi=\lambda/(3L)$ is obtained, where L is the length of the cylinder. The expression in (2.9) is suggested as a better approximation since a multicopter propeller has a different geometry than both a helicopter blade and a cylinder.

The amplitude of the RCS may be approximated using the backscattering from an infinitely long, circular cylinder with a radius a, chosen such that the volume of a cut of length L of the infinite cylinder, corresponding to the length of the propeller, encloses the same volume as the propeller [14]. An infinitely long structure does not have a RCS as the infinite geometry yields an infinite area. The scattering is instead expressed as a scattering width, which is RCS per unit length. A conversion can be made from the scattering width (σ_{SW}) of an infinite structure to the RCS (σ_{RCS}) of a finite cut of length l of the structure using the relation [25]

$$\sigma_{RCS} \cong \sigma_{SW}\frac{2l^2}{\lambda}. \tag{2.10}$$

Expressions for the amplitude of the broadside scattering width from an infinitely long, horizontally oriented cylinder have been developed [22] and are given for HH- and VV-polarisation by

$$\sigma_{HH}(0) = \frac{4}{k_0}\left|\sum_{n=0}^{\infty}\epsilon_n(-1)^n A_n\right|^2 \tag{2.11}$$

$$\sigma_{VV}(0) = \frac{4}{k_0}\left|\sum_{n=0}^{\infty}\epsilon_n(-1)^n B_n\right|^2 \tag{2.12}$$

where ϵ_n is a constant with values ϵ_0=1; ϵ_1= ϵ_2= ϵ_3=…=2, k_0 is the wavenumber in vacuum. A_n and B_n are coefficients given by the rather intricate expressions

$$A_n = -\frac{(k_1/\mu_1)J_n(k_0a)J_n'(k_1a) - (k_0/\mu_0)J_n'(k_0a)J_n(k_1a)}{(k_1/\mu_1)H_n^{(1)}(k_0a)J_n'(k_1a) - (k_0/\mu_0)H_n'^{(1)}(k_0a)J_n(k_1a)} \tag{2.13}$$

$$B_n = -\frac{(k_1/\varepsilon_1)J_n(k_0a)J_n'(k_1a) - (k_0/\varepsilon_0)J_n'(k_0a)J_n(k_1a)}{(k_1/\varepsilon_1)H_n^{(1)}(k_0a)J_n'(k_1a) - (k_0/\varepsilon_0)H_n'^{(1)}(k_0a)J_n(k_1a)} \tag{2.14}$$

where

$$k_0^2 = \omega^2 \mu_0 \varepsilon_0 \quad \text{and} \quad k_1^2 = \omega^2 \mu_1 \varepsilon_1$$
$$\omega = 2\pi f \tag{2.15}$$

for a cylinder with dielectric constant ε_1 and permeability μ_1, and a transmitted frequency f. J_n and H_n in the above equations are Bessel functions and Hankel functions respectively of the n-th order and primes denote the derivatives.

2.3.2 Electromagnetic simulation models

For analytic RCS solutions to Maxwell's equations to be feasible, the geometry of the scatterer must be sufficiently simple and, in addition, other approximations may be necessary to arrive at a tractable problem. Thus, the analytical results presented above for the RCS of thin, circular cylinders provide only coarse models for the scattering from a real propeller.

However, numerical solution of Maxwell's equations is a powerful alternative and, in particular, the finite element method (FEM) is well suited for problems with complicated geometry. For 3D problems, the FEM typically divides space into an unstructured mesh of tetrahedrons, where the electric field is represented by piecewise low-order polynomials. A system of linear equations is derived by setting the weighted residual of the differential equation to zero.

For scattering problems, the computational domain discretised by the FEM can be efficiently truncated by a so-called perfectly matched layer (PML) [26]. The PML absorbs the outward propagating scattered field efficiently and this allows for a perfect electric conductor (PEC) backing that serves as the outer boundary of the computational domain. The scattered field in the vicinity of the scatterer is transformed [27] to the far-field region, where the RCS is computed.

The PML is the most efficient at absorbing electric fields at near normal incidence to the PML. However, a wave impinging on the PML with a near tangential line of propagation (near 0° grazing angle) may be reflected at the PEC backing and propagate back into the computational domain. Thus, radiation that should have been absorbed by the PML may interact with the scattering object again. This problem is more prominent in elongated structures as the long structure promotes the effect as illustrated in Fig. 2-4.

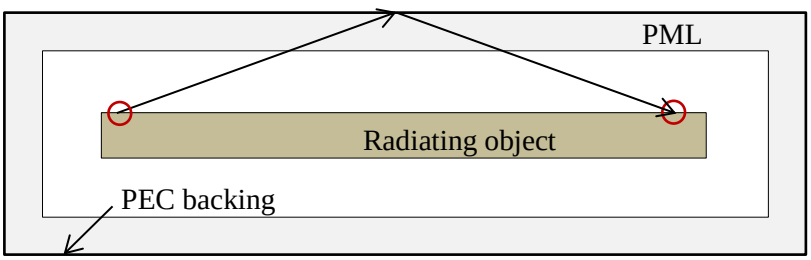

Fig. 2-4. Illustration of reflections at the PML. For simplicity, the illustration shows reflection of an optic ray whereas the actual wave behaviour may be much more complicated. Instead of being damped out by the PML, the wave reflected from the object is reflected at the boundary and it can interact with the object again.

2.3.3 Range- and cross-range profiles

A technique commonly used in inverse synthetic aperture radar (ISAR) is to create range- and cross-range profiles of a target that shows the structure of the target in radial or perpendicular direction. This technique is based on the point scatter distribution model where the location of scatter centres is derived from varying the illumination angle or the transmitted waveform and then applying the inverse Fourier transform (IFT) on the received signal.

The cross-range profile is achieved by varying the angle with which the target is illuminated. The total received signal is a sum of the signal from each point scatter centre as

$$E_s(\varphi) = \sum_{i=1}^{P} A_i e^{-j2k\cos(\varphi)x_i} e^{-j2k\sin(\varphi)y_i}, \tag{2.16}$$

where P is the number of assumed point scatterers, k is the wavenumber of the transmitted wave, A_i is the amplitude of the field from scatterer i, and x_i and y_i are the radial and the perpendicular displacement of a point scatterer i from the centre of the target. If the radial displacement of point scatterers is near constant, the term $\cos(\varphi)x_i$ is approximated as constant and (2.16) may be rewritten as

$$E_s(\varphi) = \sum_{i=1}^{P} B_i e^{-j2k\sin(\varphi)y_i} = \sum_{i=1}^{P} B_i e^{-j2\pi\frac{k}{\pi}\sin(\varphi)y_i}, \tag{2.17}$$

where $B_i = A_i e^{-j2k\cos(\varphi)x_i}$ is a constant. In (2.17) there is a Fourier relationship between $\frac{k}{\pi}\sin(\varphi)$ and y_i, thus the scattered field may be expressed as a function of y by taking the IFT of the total signal as

$$E(y) = \mathcal{F}^{-1}\{E_s(\varphi)\} \tag{2.18}$$

As $E(y)$ essentially is equal to B_i, a hypothesis is that the range profile may then be obtained by extracting the phase content of $E(y)$ and dividing by $2k$.

2.3.4 Micro-Doppler signature

The motion of an object induces a shift in frequency of a reflected wave due to the Doppler phenomenon. However, an object may be comprised of several parts with individual motion, where each part induces a specific Doppler shift. Examples of this are the rotating blades of a helicopter or the swinging arms and legs of a human. An incoming electromagnetic wave is therefore modulated by all the different Doppler shifts and the returned signal may then be analysed spectrally to find the frequency shifts of the individual parts. This effect is known as the micro-Doppler effect and the individual motion of parts is called micro motion [28].

As the micro motion often is a function of time, the micro-Doppler effect is best observed in a joint time-frequency representation as illustrated in Fig. 2-5, where the radar return of a simulated rotating cylinder is shown. There is a clear sinusoidal envelope emerging from the rotation which is due to the Doppler shifts only appearing when a point on the object is moving towards or away from the observer. In the joint time-frequency representation,

Doppler shifts appear as sidebands to the shift induced by the translational movement of the body and positive Doppler shifts indicates movement towards the observer and negative shifts indicates movement away. Therefore, one observes so-called flashes with wide spectrum width when the cylinder is observed at broadside as every point on the body is either moving towards or away from the observer. These flashes are observed at times t={0.25; 0.75; 1.25; 1.75} in Fig. 2-5.

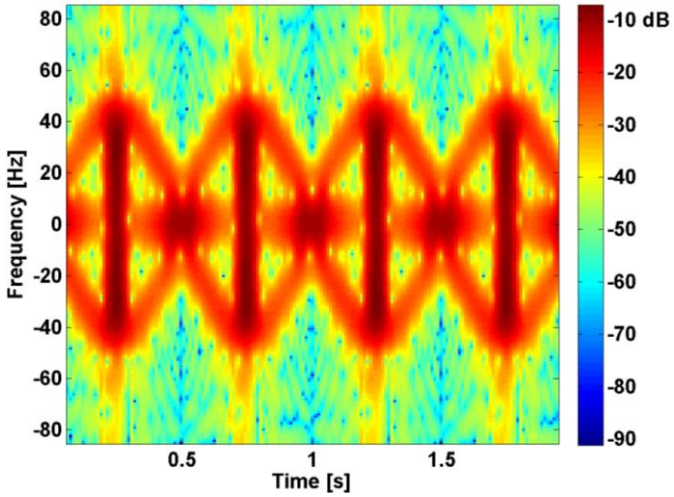

Fig. 2-5. The joint time-frequency representation of the micro-Doppler spectrum for a simulated rotating cylinder with r=5mm and L=200 mm, rotating at 1 Hz. The sinusoidal envelope is distinct and is due to that Doppler shift only occurs in the radial direction. When the rod is observed at broadside, flashes appear as many points on the rod are either approaching or receding. Two flashes are seen per complete revolution.

To obtain the micro-Doppler signature, the short time Fourier transform (STFT) is used. The Fourier transform is computed for some finite time interval and the result is used as a representation of the frequency content for that time interval. Given a sequence of such time intervals the time-frequency signature is built up from many of these STFTs.

The appearance of the signature can be changed depending on the length of the time interval of each STFT. If the time is short, the micro-Doppler signature shows the instantaneous frequency content whereas a longer time instead represents the overall frequency content which is an average over the time interval. To fully capture the motion, an overlap of the STFTs is necessary for a smooth representation. The amount of overlap needed depends on the movement being imaged and its velocity components.

2.3.4.1 Extraction of features using SVD

In order to use the micro-Doppler signature for classification it is necessary to be able to extract relevant features from it in a way such that algorithms can process the data. There are several ways to accomplish this, e.g. by principal component analysis (PCA) or independent component analysis (ICA). One simple way is to use singular value decomposition (SVD) of the data.

With SVD, a matrix A may be rewritten on the form

$$A = U\Sigma V^T, \tag{2.19}$$

where Σ is a diagonal matrix containing the singular values of A in descending order, and U and V are unitary matrices. If SVD is applied to complex time-frequency data as the one presented in Fig. 2-5, the column vectors of matrix U are coupled to the frequency data and the column vectors of V are coupled to the time data. There is also a relation to the magnitude of the singular values in Σ, where if the first singular value is large then the first vectors have the most significant data points and so on. This is used in various areas such as image compression where data points coupled to the lowest singular values are removed and thus the most significant data points are kept and important features in the image are preserved while reducing the image size.

3 STATIC RADAR RETURN OF A SINGLE PROPELLER

The use of multiple propellers is the common denominator for all multicopters and the fast speed of the propellers is a very distinct feature that has potential to be used in classification algorithms. It is therefore of great interest to know how the radar return of a single propeller may look like and whether there are models that can approximate its most important features. However, the static radar return must first be calculated to simulate a propeller in motion.

The static radar return of a single propeller is investigated by varying different properties such as the dielectric constant, polarisation, angle of illumination and carrier frequency. The simulation software used for these static calculations is Ansys HFSS, which is a finite element solver and the software is firstly described along with the setup of the calculations and the relevant parameters that can be changed. Thereafter, the different investigated cases are stated followed by the results of each case. The numerical results are then compared to analytical results that describe the RCS. Lastly, the choice of investigated cases is summarised and discussed to show which cases are spanned by this study.

3.1 RCS calculations using Ansys HFSS

HFSS is a numerical tool for the computation of electromagnetic fields in, e.g., microwave problems. It uses the three dimensional FEM where the computational domain is divided into an unstructured mesh of volume elements in the form of tetrahedrons. A solution for the electric field is computed in each volume element and the residual for each volume element is calculated. The software then uses adaptive mesh refinement in order to minimise the residuals. This means that complicated areas such as sharp edges or other singularities where the residual is large are automatically subdivided into more volume elements in order for the electric field solution to approach a continuous case. The solution reaches a steady-state when the residuals have been minimised which is based on a convergence criterion set by the user.

Analysed structures can be drawn in the program by the user in its computer aided design (CAD) environment using simple geometries. CAD models can also be imported into the program for analysis. The propeller investigated herein is not created from scratch but is instead imported into HFSS from an online database [29], where users share their created 3D models. In the simulations, different parameters can easily be varied by the usage of variables and by adding parameter sweeps.

The setup used for all static calculations in this study is illustrated in Fig. 3-1. Given a propeller (centred at the origin and aligned with the y-axis), HFSS is used to calculate the complex scattering amplitude $\vec{F}$, which gives the scattered electric field

$$\overrightarrow{E_s} = \frac{e^{-jkR}}{R}\vec{F}. \tag{3.1}$$

The RCS can then be computed based on (2.6). According to HFSS documentation, the distance D between the scattering object and the PML-air interface should be chosen such that $D>0.25\lambda$. However, a greater distance of $D=0.4\lambda$ is advised from previous experience with the software. As the propeller has internal structure, the distance D is based on the smallest

distance from the propeller to the PML which is determined by enclosing the propeller in a non-model object which is not part of the calculations and is as small as possible while still containing the structure. At the outer boundary of the air box, a layer of PML is assigned as boundary condition to simulate an infinitely large air volume and the infinite sphere tool may then be used to get the far field radar return. The propeller is then illuminated at angles -90°<φ<90° with an angular resolution of 1°, with φ=0° being at broadside and φ=±90° being at end-fire. As the propeller is symmetric looking from the front and from the back of it, the full 360° RCS is obtained by mirroring the RCS for the front side.

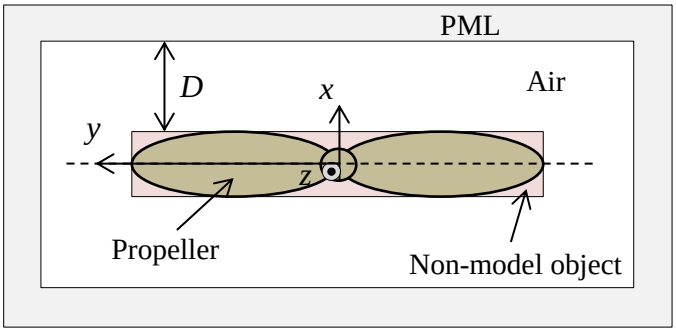

Fig. 3-1. An illustration of the setup used for calculations of the static radar return of a propeller in HFSS.

3.1.1 Setup of parameters

One of the settings relevant for RCS calculations is the setting of the PML. Here, one can change two parameters: the minimum radiating distance and the PML thickness. The minimum radiating distance is the minimum distance from a radiating body to the PML and should be set accordingly as the distance from the non-model object to the PML-air interface, i.e. the distance D in Fig. 3-1. It is although advised to choose this value to be somewhat smaller than the exact distance and it is set to $0.9D$ instead. The thickness of the PML is chosen such that unwanted radiation is damped out and experience has shown that for many cases, a thickness of 0.4λ is sufficient.

The material of the propeller is varied in the simulations. Many material parameters can be changed in HFSS ranging from different magnetic properties such as magnetic saturation and relative permeability, to dielectric constant and loss tangent. Magnetic properties are for most materials investigated herein not relevant as they are non-magnetic and are therefore neglected. The dielectric constant is set to be real only, thus neglecting losses in the material. The loss tangent in plastics is usually in the order of $\tan\delta = 0.1$ and this approximation would therefore likely not be too impactful on the obtained results.

An incident plane wave is assigned to the problem. Polarisation of the wave is set through two parameters: “E0 Phi” and “E0 Theta”. This determines the amplitude of the electric field in the $\hat{\varphi}$ and $\hat{\theta}$ directions respectively and the relation between the two amplitudes decides the polarisation. With “E0 Phi” set to 1 and “E0 Theta” set to 0 the wave becomes horizontally polarised and with “E0 Phi” set to 0 and “E0 Theta” set to -1 the wave becomes vertically polarised.

When all parameters have been set, a convergence criterion is set and the simulation is run. The criterion set for all simulations in this study is “Maximum Delta Energy”=0.005 which is a strong criterion that is believed to yield accurate results.

When results are obtained from the simulations, the received polarisation can be changed. This is done through choosing data points “ComplexMonostaticRCSPhi” for the complex field received in horizontal polarisation and “ComplexMonostaticRCSTheta” for data received in vertical polarisation.

3.1.2 Effects of PML reflections and error estimation

As the propeller is an elongated structure, it may cause reflections in the assigned PML boundary condition. This is therefore tested by increasing the smallest distance D between the propeller and the PML in three steps, D={0.4λ; 0.6λ; 0.8λ}. The different parameters of this test case are chosen such that they represent a typical propeller in the calculations presented later in this report so that the test may result in relevant error estimation. A representative dielectric constant and frequency are chosen for the test as ε_r=8.0 with frequency f=10 GHz as the material is rather reflective and the frequency gives the smallest wavelength and, therefore, yields the smallest values of D and smallest grazing angles α. Polarisation is chosen as HH-polarisation. A 9” or 23 cm diameter propeller is used which is 7.63λ long expressed in wavelengths at this frequency. This means that the near-grazing angles tested for these distances then are α={6.0°; 8.9°; 11.9°} for a reflection point at air-PML interface as it intersects the plane y=0. The result of the calculations can be seen in Fig. 3-2. Little difference is seen as D is increased and this suggests that the adaptive meshing or PML dampening of HFSS is taking care of the issue of PML reflections. A few angles are identified where the difference is the largest and the RCS for these angles are summarised in Tab. 3-1. The angles are chosen such that they are not located in deep minima since the largest fluctuations are expected at such angles due to the low RCS values. The largest change in RCS is 1.45 dB, whereas there is almost no difference for most azimuth angles.

As the increased distance D did not show large fluctuations in RCS, D=0.4λ is deemed to be accurate, which also is in good agreement with previous experience of the software. Therefore, the smaller air volume with D=0.4λ is used for simulations carried out within this study.

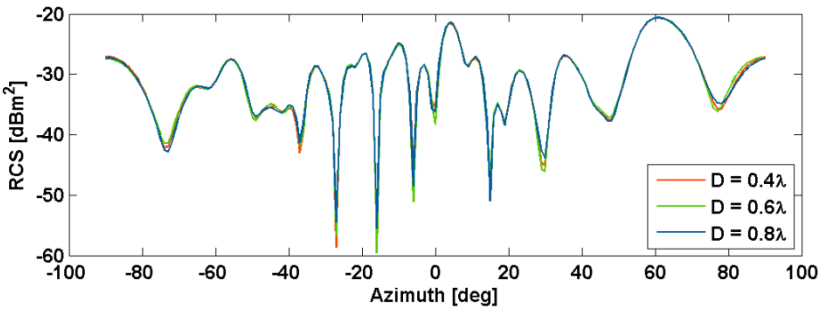

Fig. 3-2. The impact of the minimum distance D from the propeller to the air box boundary on the RCS, with ε_r=8.0 and f=10 GHz. 0° is at broadside of the propeller. There is not much variation observed in the main lobes. The largest variation is seen in the deep minima as they are sensitive to changes due to the low RCS values.

Tab. 3-1. Calculated RCS in dBm^2 for a few identified angles where the change in RCS is large, as the distance D from the propeller to the boundary of the air box is increased. The largest change is seen for φ=-73° where the RCS changes by 1.45 dB from D=0.6λ to D=0.8λ.

	φ = -73°	φ = -45°	φ = -40°	φ = 47°	φ = 77°
D = 0.4λ	-42.00	- 35.43	-35.69	-37.51	-35.72
D = 0.6λ	-41.40	-34.96	-35.55	-37.10	-36.21
D = 0.8λ	-42.85	-35.52	-35.17	-37.74	-34.76

As a final test, a reference case for RCS calculations consisting of two dielectric spheres of radius 15 cm and at a distance of 4 m apart is used. The dielectric spheres have the permittivity ε_r=1.5-0.02/($j2\pi f\varepsilon_0$). An electromagnetic wave impinges on one of the spheres along the axis of the two spheres and the monostatic RCS is calculated at frequencies 5 MHz to 4 GHz in steps of 5 MHz with a T-matrix solution method including multiple scattering. The setup of the reference case is shown in Fig. 3-3. This scenario is modeled in HFSS and calculated for the relevant frequencies with the parameters D=0.4λ, minimum radiating distance of the PML as 0.9D and thickness of the PML as 0.4λ. However, the reference case features a distance of 4 m between spheres and the problem investigated herein is 23 cm long. Thus, it is necessary to scale the frequency in order to make the distance in wavelengths between the spheres equal to the length of the propeller in wavelengths. Rescaling the frequency with a factor of 0.2/4=1/20 gives the new frequencies f={50; 150; 300; 500} MHz for the reference case and this corresponds to f={1; 3; 6; 10} GHz, respectively, for a typical propeller considered in this thesis. In addition, the list of frequencies is extended such that f={45; 50; 55; 135; 150; 165; 270; 300; 330; 450; 500; 550} MHz. The result of the test is presented in Fig. 3-4 and it shows good agreement with the reference data with a deviation less than 1 dB for most frequencies. At 55 MHz, however, there is a difference of 5 dB and, also, the RCS is very low at this frequency. Thus, spurious reflections at the PML-air interface may change the RCS substantially.

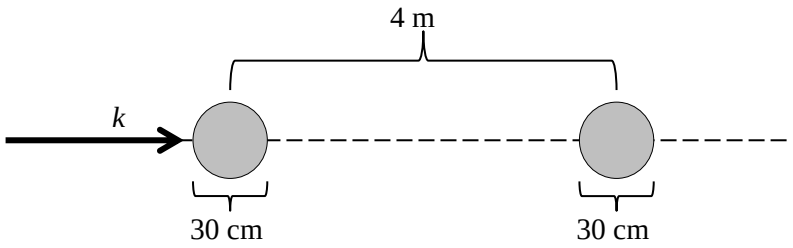

Fig. 3-3. The setup of the RCS calculation reference case. The two spheres have a dielectric constant of ε_r=1.5-0.02/($j2\pi f\varepsilon_0$) and the wave vector is aligned with the straight line through the centres of the two spheres.

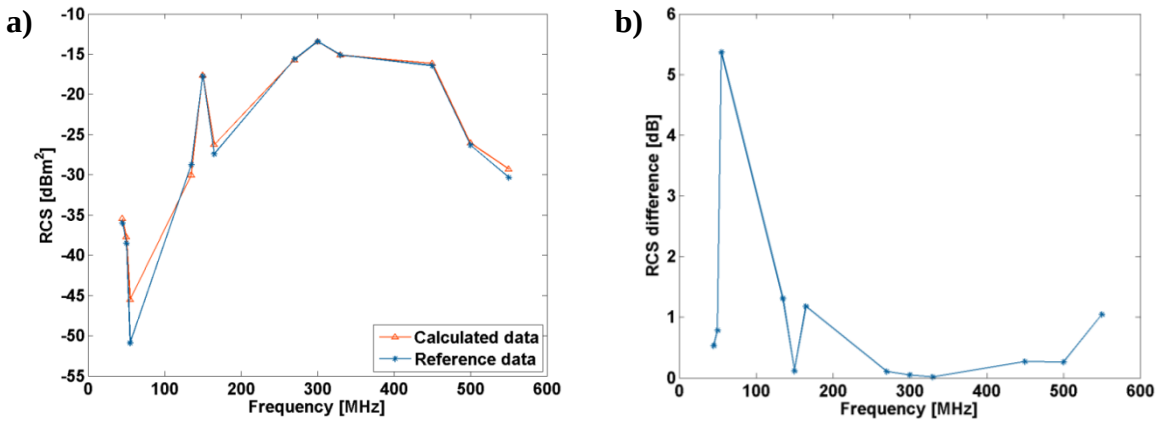

Fig. 3-4. **a)** Test of the setup in HFSS in comparison to reference data and **b)** the absolute value of the difference between the two RCS datasets.

3.2 Propeller characterisation and property variations

Multicopter propellers come in all different sizes and shapes. To study how different properties affect the radar return without having to simulate each possible configuration, a set of representative cases is defined.

In order to show the dependence of RCS on the material of the propeller, five different dielectric constants are chosen. Inspiration is taken from [30] where dielectric constants of plastics have been measured at a low frequency of 1 MHz. Thus, dielectric constants ε_r=3.4 and ε_r=5.7 are chosen which are the dielectric constants at low frequencies for nylon 6,6 and a glass reinforced plastic which are materials that could be used in multicopter propellers. This should however not be interpreted as their dielectric constants at higher frequencies as they are only accurate at the measured frequency but they are chosen nevertheless as no data at relevant frequencies could be found. A higher dielectric constant of ε_r=8.0 is chosen as well. Inspiration is here taken from [31] where the dielectric properties have been measured once again at lower frequencies of up to 0.5 MHz for carbon fibre in epoxy resin composite material. The dielectric constant was observed to be high at about ε_r=8.0 for 15wt% of carbon fibre and increased with increased wt%. It has also been shown that carbon fibre materials are almost as reflective as aluminium at radar frequencies, despite being much less conductive [32], which indicates that a high ε_r may be expected at higher frequencies. Also, two extreme cases were picked with ε_r=2.0 and PEC which could be seen as having an infinite dielectric constant and is henceforth referred to as ε_r=∞. These dielectric constants could represent wood which is largely transparent and a metal which is highly reflective. Propellers made out of wood and metals are uncommon but are alternatives that are used in some cases.

Frequency and polarisation are varied as well. The chosen radar operating frequency bands are the ones most common within search and track radar systems: L-, S-, C- and X-band. To limit the number of investigated frequency cases, one representative frequency per frequency band was chosen as 1 GHz, 3 GHz, 6 GHz and 10 GHz, corresponding to wavelengths 30 cm, 10 cm, 5 cm and 3 cm. Polarisation is chosen as VV- or HH-polarisation as they are common within these radar applications. The elevation angle is also varied to investigate whether the radar return varies with angle of illumination.

The CAD-models of the propellers are taken from an online database [29], thus sizes and shapes of the propellers are limited to what is freely available. Available sizes range from 5" to 26" and a 9x4.7", CCW propeller model is chosen as the base for the computations as the model seems to be well made and accurate and of a typical size for small or medium sized multicopters. The CAD-model is shown with its orientation in the problem setup in Fig. 3-5 and this model is used in all the following simulations unless it is stated explicitly that another propeller model is used. The dimensions of the red, non-model box enclosing the CAD-model are 32x230x11 mm and roughly gives the dimensions of the propeller.

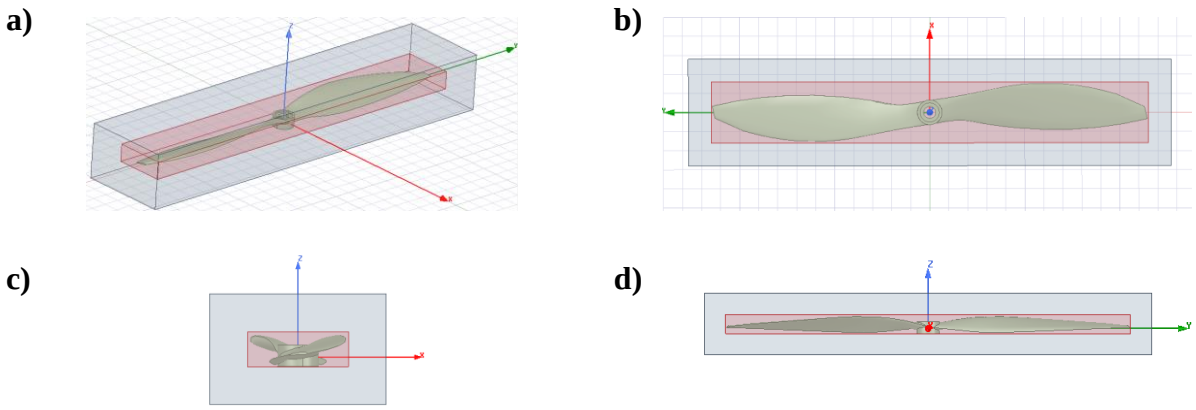

Fig. 3-5. The 9x4.7" CAD-model used in most simulations and its orientation in simulations, viewed from: **a)** 3D view; **b)** top view; **c)** side view; and **d)** front view.

3.2.1 Basic case: HH- and VV-polarisation

The two computed polarisations are HH-polarisation and VV-polarisation which are common in radar applications. This is calculated for dielectric constant ε_r=8.0 at 10 GHz and the results are shown in Fig. 3-6. Vertical polarisation RCS is approximately 8 dB smaller than the horizontal polarisation at most angles. Furthermore, the vertical polarisation yields a 17.2 dB smaller RCS at broadside as compared to the horizontal polarisation. This is expected since the propeller is much larger in the horizontal direction, with its total length of 23 cm than it is in the vertical direction with its height of approximately 1 cm.

The vertical polarisation results in smaller RCS than horizontal for this kind of structure which is in good agreement with [13] and [14]. As there is such a great difference in RCS between the two polarisations, HH-polarisation is used in the following simulations if nothing else is stated since a larger RCS is beneficial for detection of a target with radar.

A calculation was also performed with ε_r=3.0 to compare with a previously calculated case with VV-polarisation in [14]. The two cases did however not fully agree and more details about this comparison can be found in Appendix A.

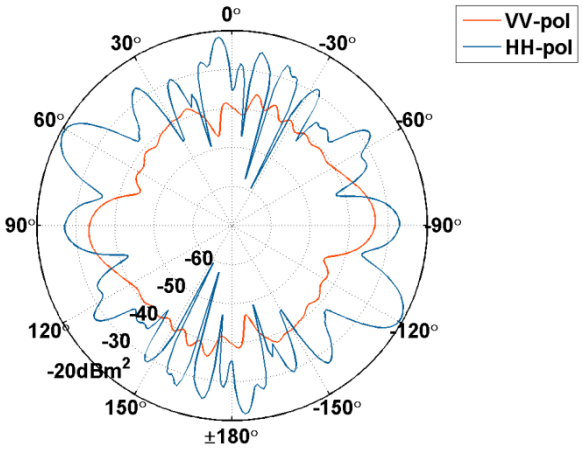

Fig. 3-6. Calculated RCS of the 9x4.7" propeller with ε_r=8.0 for HH- and VV-polarisation. VV-polarisation is notably smaller than HH-polarisation by on average 8 dB and by 17.2 dB at broadside.

3.2.2 Variation of material and carrier frequency

To see how different materials of propellers may look like at different radar bands, a variation of the two parameters is performed. The result of the three mid-range values of dielectric constant, ε_r={3.4; 5.7; 8.0}, is shown in Fig. 3-7. At lower frequencies 1, 3 and 6 GHz there is a distinct lobe at around 0° (broadside) and there is almost no energy radiated at ±90° (end-fire). This can be intuitively expected as the propeller is structurally much larger when viewed at broadside, which should also be reflected in its RCS at this angle. However, at the higher frequency of 10 GHz, significant lobes at end-fire are also observed which are comparable to, and may even be larger than, the lobe at broadside. The end-fire lobe is also shifted to 60° instead of 90° as ε_r is increased. The large end-fire lobe is predicted for long, thin bodies illuminated at end-on incidence with HH-polarised radiation, where backscattered energy appears to radiate from the rear of the body [22]. Another contributing factor may be that the propeller has become much longer than the wavelength. The length of the propeller expressed in wavelengths for each of the frequencies is 0.76λ, 2.29λ, 4.58λ and 7.63λ, where the latter approximately fulfils the condition L=7.63$\lambda \gg \lambda$. As a consequence, four RCS flashes per full revolution of the propeller may be observed at 10 GHz as opposed to the two flashes normally seen for elongated structures such as the rotor blades of a helicopter.

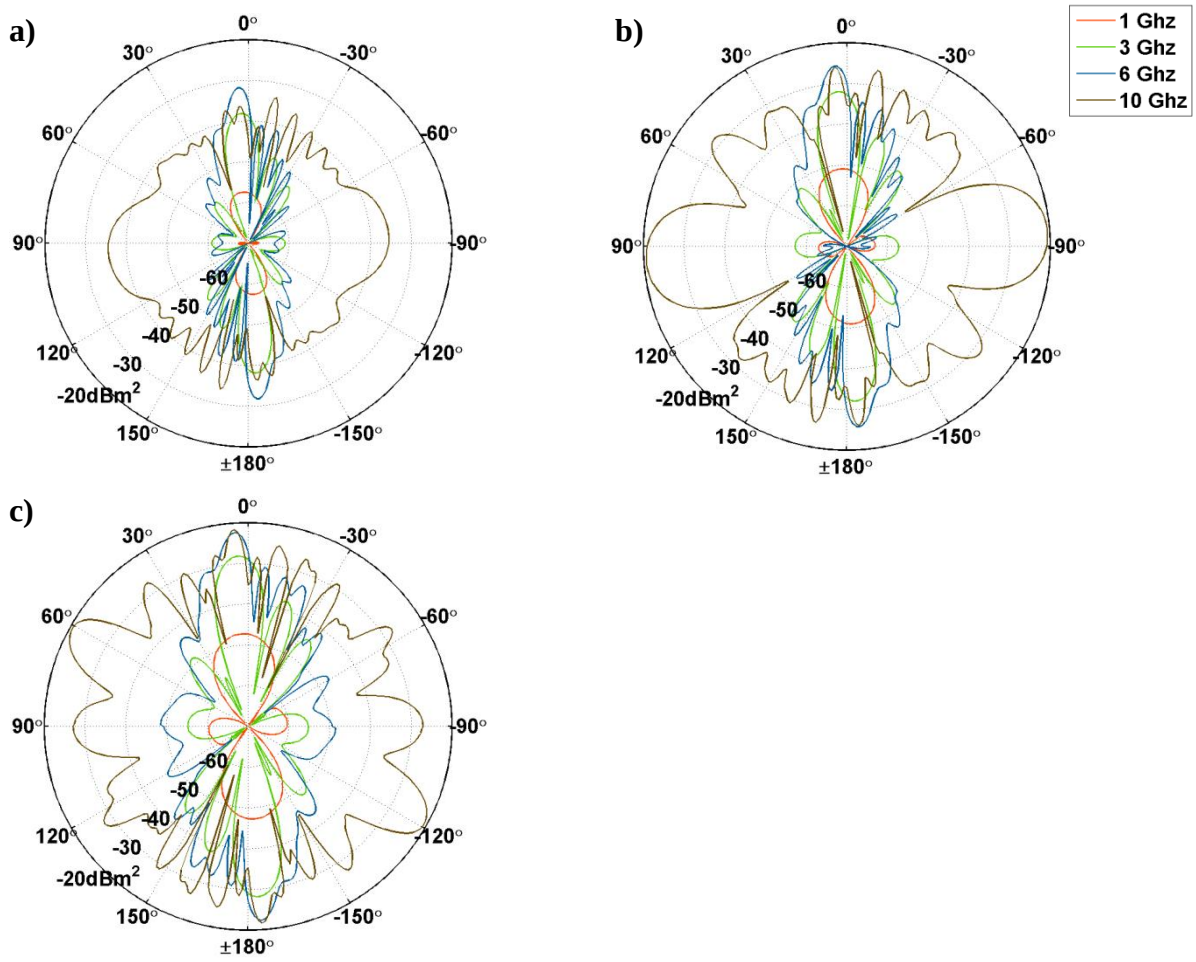

Fig. 3-7. RCS of the 9x4.7" propeller at different frequency bands for dielectric constants: **a)** ε_r=3.4; **b)** ε_r=5.7; and **c)** ε_r=8.0. For 1, 3 and 6 GHz the broadside RCS is much larger than end-fire RCS as expected. At 10 GHz however, end-fire RCS is comparable to, or even larger than, broadside RCS.

Looking at the broadside lobe for the different cases there are some general patterns that can be observed. The maximum of the lobe is not always aligned with 0° and this is due to the geometry of the object. From the amplitudes of the RCS, it is clear that the RCS is very low for 1 GHz, where it is approximately 25 dB lower than at other carrier frequencies for all three cases. The long wavelength suggests that the problem is approaching the Rayleigh region in all dimensions of the propeller at this frequency and the RCS may therefore be expected to decrease quickly with decreased frequency. The frequencies 6 and 10 GHz yield the highest amplitudes and their amplitudes are also comparable to each other at broadside, whereas 3 GHz gives a slightly smaller RCS with about 6 dB reduction. The broadside lobe widths are calculated as the half-power lobe width given that the angular resolution is 1°. An estimate with improved angular resolution is made by linearly interpolating between data points. The lobe width is seen to be decreasing with increased frequency, which is predicted in (2.9).

The two special cases of ε_r={2.0; ∞} are also calculated and the results can be seen in Fig. 3-8. Unsurprisingly, the RCS values for ε_r=2.0 are very low at below -40 dBm^2 at all frequencies and all aspect angles, which is due to the low dielectric constant. For ε_r=∞ the

pattern becomes more complicated with many side lobes for lower frequencies as well. The end-fire RCS lobes are shifted from 90° to 60° (as in the case with ε_r=8.0 at 10 GHz) which can be observed at frequencies 3, 6 and 10 GHz. This behaves much like the RCS of a thin PEC cylinder, as studied in [14], where the same type of side lobes at 60° are seen. The amplitude is in this case increasing with decreasing frequency, which is the opposite behaviour from the cases in Fig. 3-7 and Fig. 3-8a). The increase in RCS at broadside between the frequencies 1 and 3 GHz is 0.8 dB, between 3 and 6 GHz is 2.7 dB and between 6 and 10 GHz is 2.7 dB. At 1 GHz, it shows almost the same characteristics as a half-wave dipole antenna which is due to the PEC material and the length of the propeller being 0.76λ at this frequency.

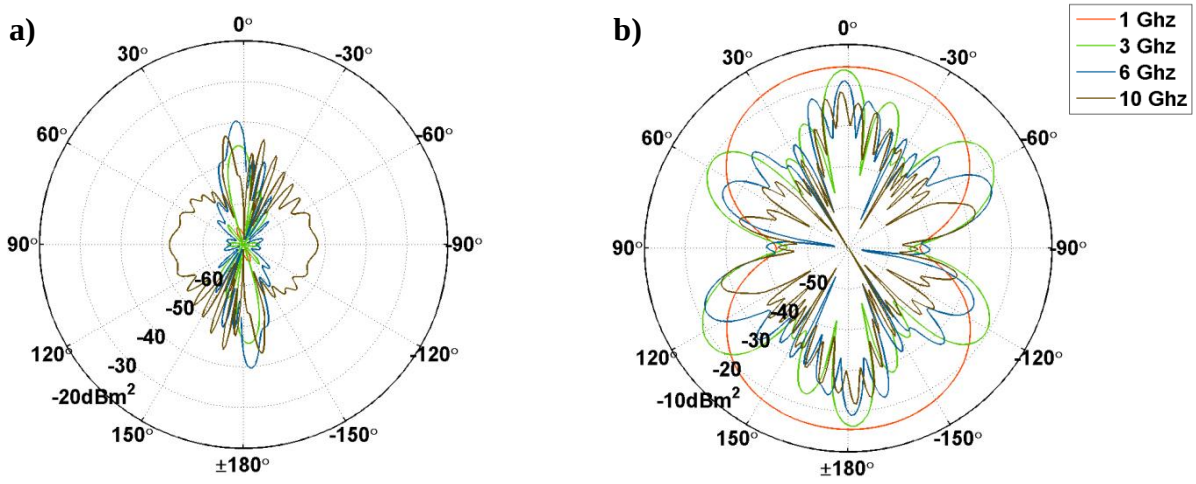

Fig. 3-8. RCS of the 9x4.7” propeller at different frequency bands for the two special cases of dielectric constants: **a)** ε_r=2.0; and **b)** ε_r=∞. The amplitude of the RCS for ε_r=2.0 is lower than -40 dBm^2 at all angles and frequencies. For ε_r=∞, the pattern is much different from other dielectric constants and is seen to increase with decreasing frequency until it at 1 GHz behaves much like a dipole antenna.

A more detailed characterisation of the radiation patterns of all material cases can be found in a table in Appendix B where the lobe widths and amplitudes are presented for the aspect angles with the largest lobes. A comparison of the calculated broadside lobe widths with the theoretical model in (2.9) is summarised in Tab. 3-2, where a good agreement is seen at all frequencies except for 1 GHz.

Tab. 3-2. The calculated broadside lobe widths for the five dielectric constants in comparison to the theoretical value based on antenna theory. A good agreement is seen at higher frequencies, whereas 1 GHz has the highest deviation for all ε_r.

Frequency [GHz]	**Calculated lobe width [°]**					**Theoretical lobe width ($\Delta\varphi=\lambda/(2L)$) [°]**
	ε_r=2.0	**ε_r=3.4**	**ε_r=5.7**	**ε_r=8.0**	**ε_r=∞**	
1	56.1	45.6	40.4	38.7	75.5	37.6
3	12.5	12.6	12.6	12.7	10.5	12.5
6	7.0	7.0	7.0	7.1	5.6	6.3
10	2.9	3.4	4.1	4.5	3.4	3.8

3.2.3 Sensitivity to frequency variation

It is evident from previous calculations that the radar return varies greatly with frequency. To capture how sensitive the RCS of the propeller is to a small frequency fluctuation, a test is performed where each of the tested frequencies were increased by 10%. The result of this test is shown in Fig. 3-9. An extra frequency calculation is added to 10 GHz as the 10% increase is such a large step, going from 10 GHz to 11 GHz. For the lower frequencies of 1 and 3 GHz, there is only a small increase in RCS with increased frequency. However, at 6 GHz, large end-fire lobes are forming with an increase of 14.0 dB at 90° from 6 to 6.6 GHz, although still considerably smaller than the RCS at broadside. This sensitivity is attributed to the problem being in the Mie region. Thus, RCS may change also for small changes in frequency. For the 10 GHz variation, the RCS amplitudes remain somewhat constant while different lobes in the radiation pattern are instead seen to shift to other aspect angles. The narrow lobe width for the broadside RCS is also becoming more difficult to distinguish as the nearest neighbouring side lobe at 10° starts to merge with the broadside lobe at 4°.

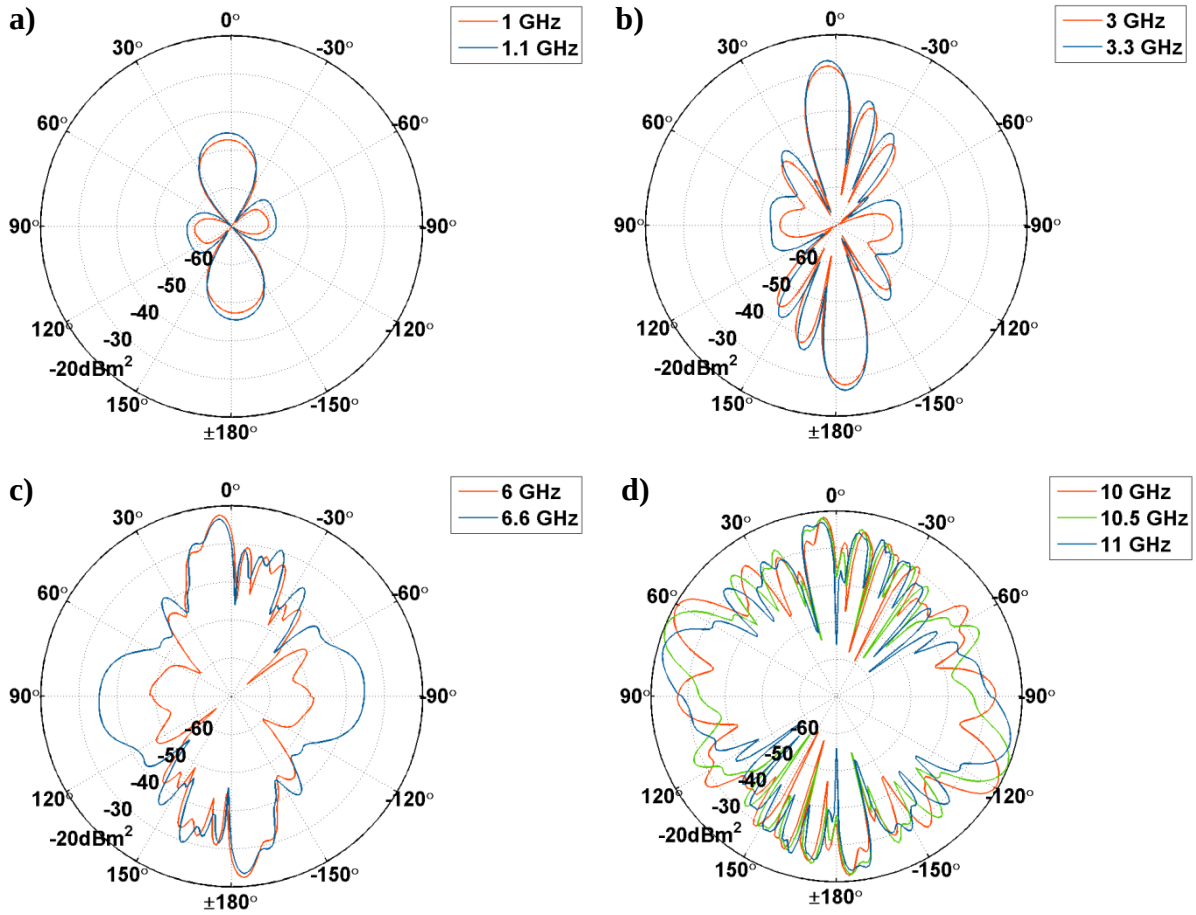

Fig. 3-9. Test of the sensitivity to frequency changes for a 9x4.7” propeller with ε_r=8.0. A change in frequency of +10% was applied to frequencies: **a)** 1 GHz; **b)** 3 GHz; **c)** 6 GHz; and **d)** 10 GHz. An extra frequency was tested for 10 GHz for better visualisation. At 6 GHz, the end-fire lobes are increasing significantly by 14.0 dB which is attributed to the problem being in the Mie region. For 10 GHz it is seen that the broadside lobe at 4° merges with the lobe at 10° as frequency is increased.

3.2.4 Elevation angle variation

As the multicopter may tilt as much as 40° during acceleration, it is interesting to analyse whether there is any change in RCS of a propeller as it is illuminated at higher elevation angles θ. Angles are therefore varied from $50° \leq \theta \leq 130°$ in steps of 20°, with θ=90° being the horizontal plane. This is also done for VV-polarised radiation as it is believed that this may yield larger RCS at end-fire as the length of the propeller is more in the vertical dimension at higher elevation angles. The result of this variation for ε_r=8.0 at 6 GHz is shown in Fig. 3-10. With HH-polarisation, there is only a slight difference that can be seen at different elevations. In VV-polarisation, the difference is more apparent at both broadside and end-fire. At end-fire, RCS is seen to be larger, as expected. At broadside however, RCS is also seen to increase at higher elevation angles. This is most likely due to the problem being in the Mie region.

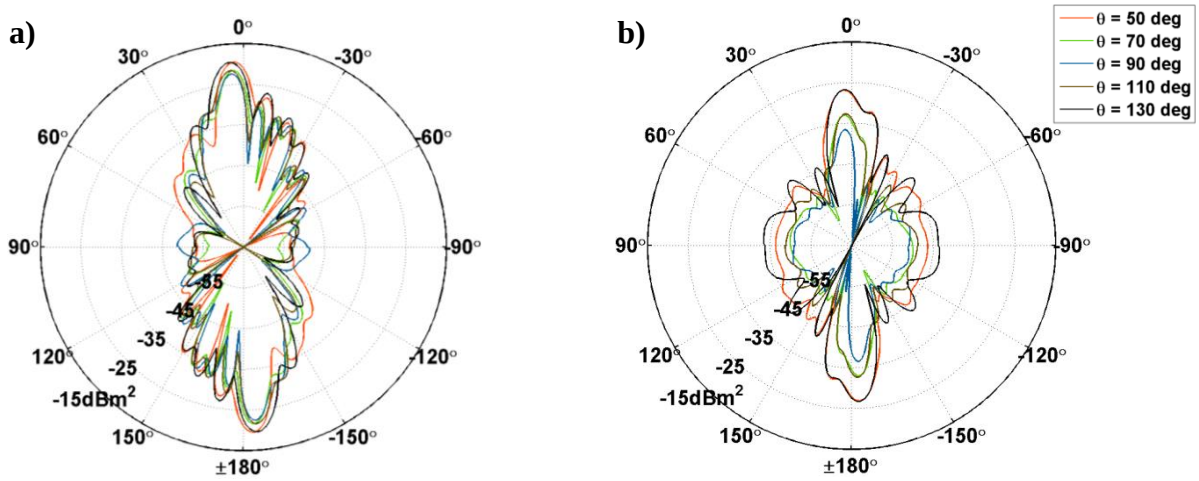

Fig. 3-10. RCS of a 9x4.7" propeller with ε_r=8.0 and f=6 GHz for different elevation angles $50° \leq \theta \leq 130°$ and two different polarisations: **a)** HH-polarisation; and **b)** VV-polarisation. With HH-polarisation there is only a slight difference whereas for VV-polarisation the RCS at end-fire is increased at high angles due to the polarisation being along the blade length. There is also a large increase of RCS at broadside which is due to the problem being in the Mie region.

In Fig. 3-11, the result of the elevation variation at 10 GHz is presented. This shows a more complex appearance of the RCS for HH-polarisation at different elevation angles. However, the amplitude levels are roughly the same except at end-fire where the RCS decreases for the highest angles θ={50°; 130°}. For VV-polarisation, the same increase of RCS at broadside as seen at 6 GHz is evident. In this case, this may be attributed to the geometrical shape of the propeller being more important at this frequency such that an incoming wave impinges on a specular reflex on its curvature, returning more energy to the source. The hole, with which the propeller is fastened to a rotating axis, also becomes more visible at higher elevation angles and effects such as cavity resonances may occur. These cavity resonances are however not seen in a real case as the hole is closed. At end-fire, a decrease in RCS is seen at higher angles. This is attributed to the shorter wavelength used and therefore the internal structure is of more importance and may reflect radiated energy in unexpected directions.

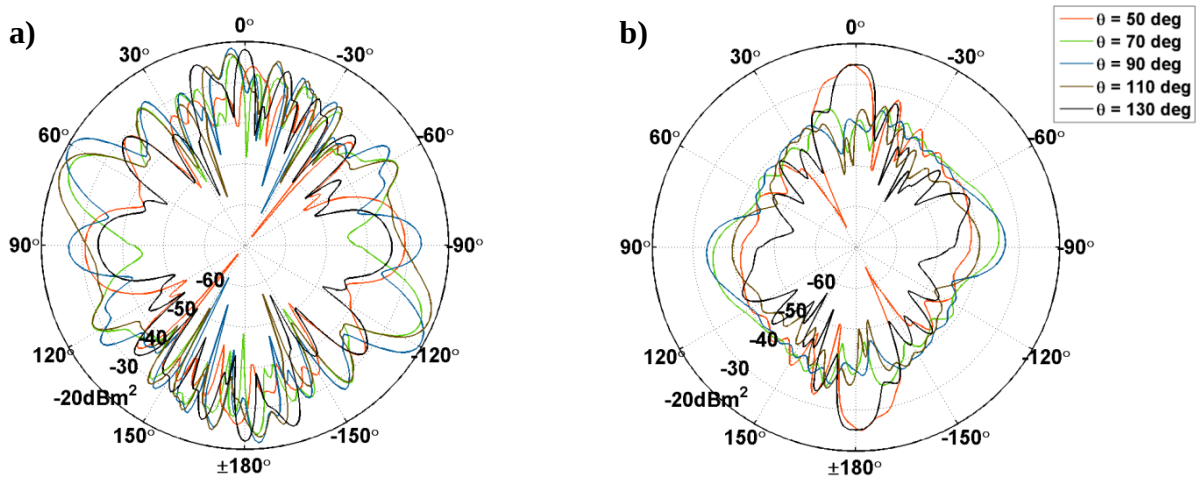

Fig. 3-11. RCS of a 9x4.7" propeller with ε_r=8.0 and f=10 GHz for different elevation angles 50°≤θ≤130° and two different polarisations: **a)** HH-polarisation; and **b)** VV-polarisation. HH-polarisation shows a complex behaviour, although with rather similar amplitude levels, except at end-fire for high elevation angles. VV-polarisation shows a higher broadside RCS for high elevations which is due to the geometry of the propeller. The end-fire RCS is also higher at low angles θ=90±20°.

3.2.5 Ducted propeller

As previously mentioned, ducts may be used on multicopter models for protecting the rotating propellers. This could potentially be an issue for radar detection as incoming radiation is scattered at the duct, without interacting with the rotating propeller, thus not generating a clear micro-Doppler signature. Therefore, the impact of the duct is calculated.

The model used in the duct calculations is shown in Fig. 3-12 with the 23 cm propeller as a reference. The thickness of the cylinder which represents the duct is set to 1 cm, outer radius to 14 cm and height to 3 cm. These parameters were chosen in order to mimic the duct dimensions seen in the Parrot AR Drone 2.0, which can be seen in Fig. 2-1a). The cylinder is also divided into segments as experience shows that perfectly smooth, curved surfaces introduce errors in calculations in HFSS and the number of segments is set to 45. The material of the duct for the Parrot model is most likely Styrofoam as it is intended for indoor use. The dielectric constant of Styrofoam has been measured to around ε_r=1.03 at a near 10 GHz frequency [33] and this is the value used in these calculations as well. Furthermore, one can imagine a worst case scenario in which a duct is made out of a more reflective material, thus ε_r=8.0 is also studied. The radar return is also calculated both with and without a 23 cm propeller with ε_r=8.0 and, in all cases, the elevation angle θ for the incident wave is set to 90° which gives incidence in the xy-plane and the frequency is set to f=10 GHz.

The results of the HFSS calculations can be seen in Fig. 3-13. The RCS of the ε_r=8.0 duct without propeller is rather high at -18±0.5 dBm^2. The small deviation of the RCS is due to the segmented cylinder and each of the peaks is seen where a segment is located. This deviation could be removed by increasing the number of segments, however the rather large increase in computational volume of this problem makes convergence harder to achieve. In the case of ε_r=1.03 it is clear that the RCS is very low at -51 dBm^2 which is expected as the low dielectric constant is almost the same as that of air which is close to 1. Large deviations of

approximately 5 dB are observed at φ={-90°; 0°; 90°; 180°}. This is where the duct is at the closest distance from the surrounding box of air and these effects may be due to the complicated wave propagation with reflections between duct and PML in conjunction with the low RCS values where small differences in absolute value may yield large differences in decibel.

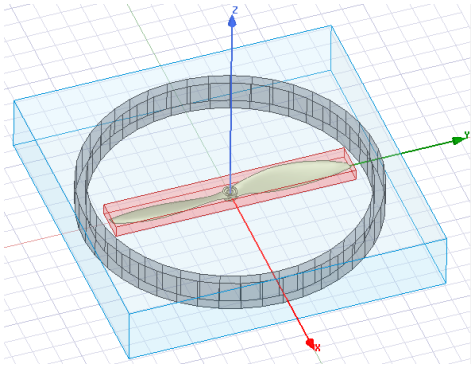

Fig. 3-12. The HFSS-design model used in calculations of the radar return from ducts. The 23 cm propeller is sometimes used in calculations as well.

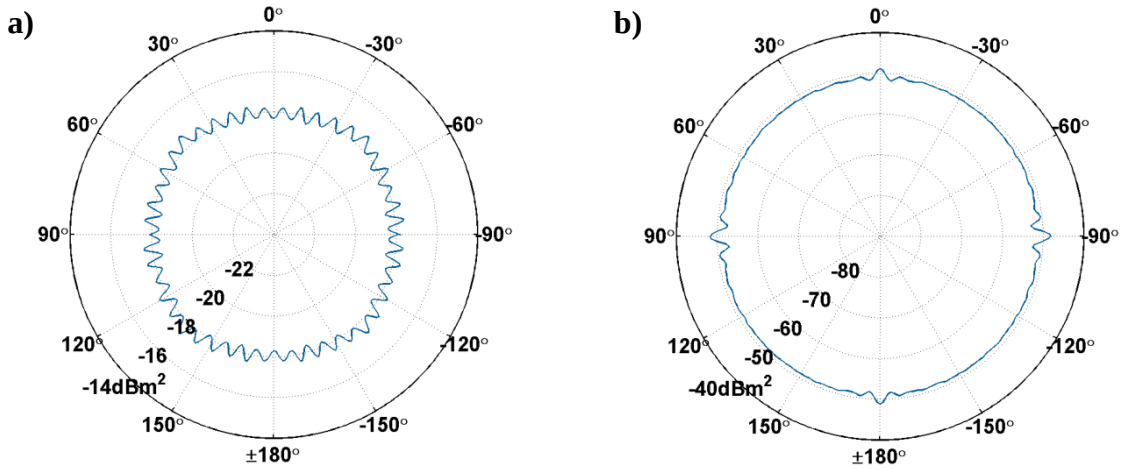

Fig. 3-13. RCS of ducts with dielectric constants: **a)** ε_r=8.0; and **b)** ε_r=1.03. The variations are due to the duct being split up into 45 segments. The scale has been chosen to show the variations more clearly.

The low RCS of the duct with ε_r=1.03 suggests that the propeller is still visible through the walls whereas the high RCS of the ε_r=8.0 duct would make it difficult to distinguish anything within it. Simulations were carried out with the duct and propeller simultaneously and the results of these tests confirm these theories and can be seen in Appendix C. The duct with the high dielectric constant is seen to almost completely shadow the propeller while the duct with the low dielectric constant reveals the propeller in detail. However, even though ducts may cover the propellers completely at horizontal incidence of an electromagnetic wave they are most likely visible as the multicopter accelerates as they may be substantially tilted.

3.2.6 Variation of propeller length

The length of the propeller is also varied in order to further investigate the length dependence on the radar return. Two additional CAD-models were chosen for this test, a 10x4.7” model

and an 11x4.7” model being 25.5 cm and 28 cm long respectively. These models were chosen as they were made using the same method for shaping the propellers to get correct aerodynamic properties. In addition, the propeller models have the same pitch, which makes comparisons easier. The angular resolution of φ is here set to 0.5° instead of the previous 1° as narrower lobe widths are expected in these calculations.

The results of the test are seen in Fig. 3-14. The radiation patterns are seen to vary, however with roughly the same shape. At 10 GHz for the 11” propeller, there is an unexpected decrease of radiation at around 0° and the largest broadside flash is seen at 11° in comparison to 4° and -1° for the 9” and 10” propellers respectively. There is also a change in the radiation at 6 GHz for the 11” propeller as the broadside flash is seen to merge with the nearest side lobe, thus getting a wider lobe width than expected. These unexpected deviations are attributed to the change in CAD-model which could introduce additional changes to the radiation pattern due to slightly different meshing of the models.

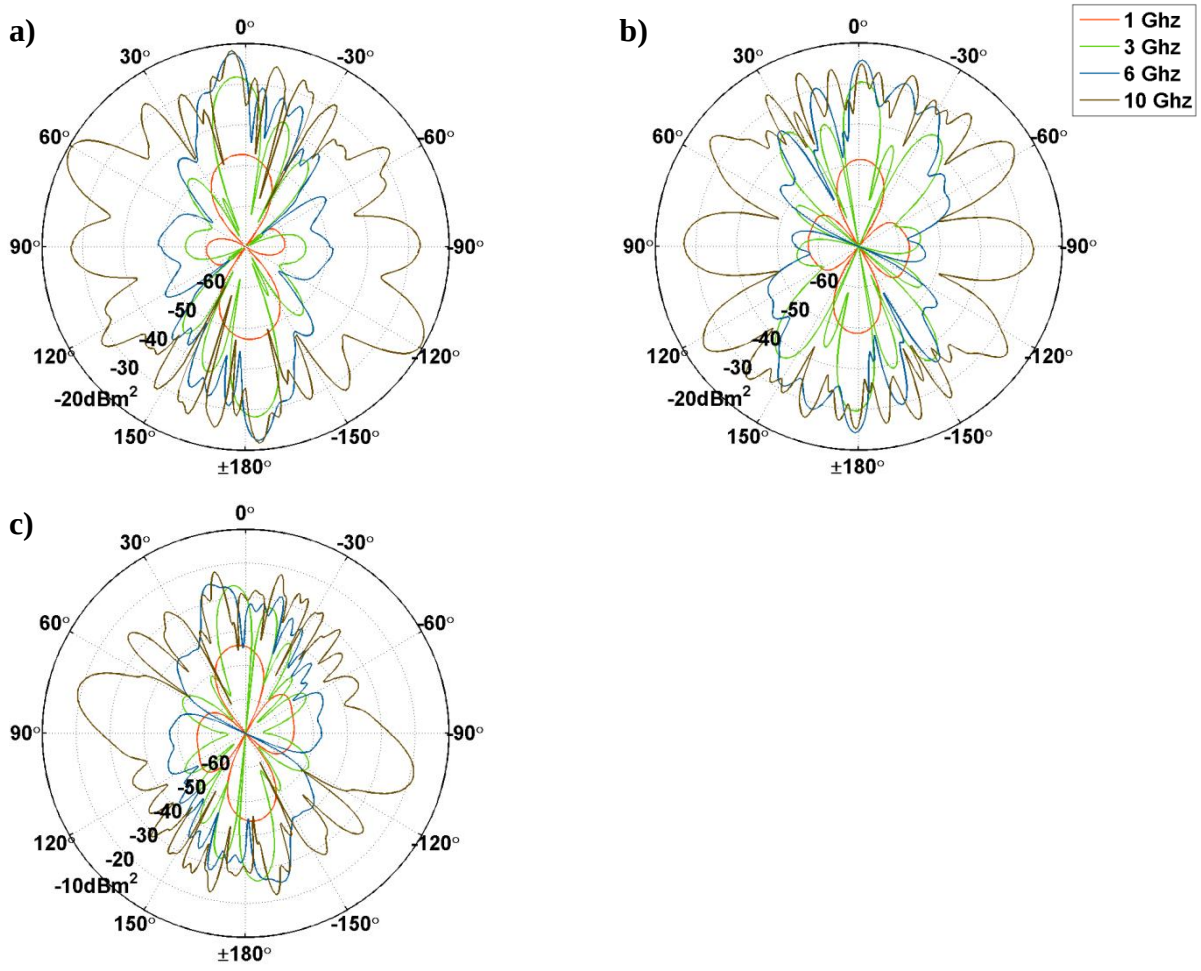

Fig. 3-14. Variation of propeller length with ε_r=8.0 and models: **a)** 9x4.7”; **b)** 10x4.7”; and **c)** 11x4.7”. The broadside lobe width is decreasing with propeller length as expected.

The lobe widths are compared to the theoretical prediction in (2.9) for frequencies f={3; 6; 10} GHz and illustrated in Fig. 3-15. The calculated lobe widths follow the predicted values quite closely with a maximum deviation of 0.87° except for the 11” model at 6 GHz where a

large deviation is observed. This deviation originates in that the lobes at broadside are merging together as mentioned above.

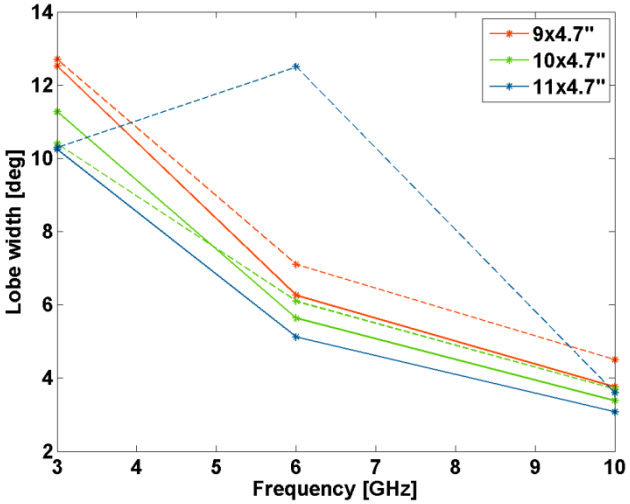

Fig. 3-15. Lobe widths ρ for different propeller lengths calculated in HFSS compared to the theoretical prediction $\rho=\lambda/(2L)$. Dashed lines are calculated values from HFSS and solid lines are predicted values. The large deviation at 6 GHz and 11x4.7” is due to two peaks merging together in RCS.

3.3 Approximation models

It is of interest to find ways to approximate the radar return of multicopters using simple models. One such way is to use a thin, circular dielectric cylinder as an approximation of the propeller, which has been previously proposed [14]. This may be used to give an upper limit of the RCS at broadside, where the propeller generates the largest flash in its micro-Doppler signature.

A Matlab script based on (2.11) is used to calculate the RCS of a finite length thin dielectric cylinder at the different frequencies and materials used in this study. The cylinder is given the same length as the propeller, i.e. 9” or 23 cm, and the radius is set such that the volume of the cylinder matches the volume of the propeller and, from previous estimates, the radius is set to 3 mm. Results of the thin cylinder are compared to the broadside RCS calculated in HFSS in Section 3.2.2 and are summarised in Tab. 3-3. It is seen that the thin dielectric cylinder model is overestimating the RCS at 6 and 10 GHz with an average of 4.0 and 11.4 dB respectively. However, at frequencies 1 and 3 GHz, the model slightly underestimates the RCS by an average difference of -3.1 dB for both frequencies. This suggests that the cylinder model may be used as an upper limit of the RCS at higher frequencies, whereas at lower frequencies it goes towards a prediction which is within approximately 3 dB of the real value. This model may therefore be seen as a good qualitative model since it roughly predicts the overall behaviour of the broadside RCS for a multicopter propeller.

The expression for the lobe width of the broadside RCS has in previous sections been studied and shown to be a good prediction. This was shown both for variations in length, wavelength and materials. This shows that in approximating the electromagnetic response of a multicopter UAV propeller, the thin dielectric cylinder model may be used to give an estimate of the

amplitude of the broadside RCS and the expression in (2.9) may predict the lobe width of the broadside RCS.

Tab. 3-3. Broadside RCS with HH-polarisation from HFSS compared to values calculated with (2.11), using radius $r=a$=3 mm and length L=23 cm. The difference shows how much the cylinder model overestimates the RCS in comparison to the calculated values for a propeller. Average differences at each frequency f={1; 3; 6; 10} GHz are {-3.1; -3.1; 4.0; 11.4} dB respectively.

ε_r	Frequency [GHz]	Cylinder approx. [dBm^2]	Calculated value (propeller) [dBm^2]	Difference [dB]
2.0	1	-68.1	-65.5	-2.6
	3	-49.8	-45.7	-4.1
	6	-36.7	-39.6	2.9
	10	-28.8	-43.7	14.9
3.4	1	-60.4	-57.4	-3.0
	3	-41.9	-38.1	-3.8
	6	-28.5	-31.7	3.2
	10	-20.3	-33.6	13.3
5.7	1	-54.5	-50.9	-3.6
	3	-35.7	-32.0	-3.7
	6	-21.6	-25.6	4.0
	10	-14.2	-26.1	11.9
8.0	1	-51.0	-47.2	-3.8
	3	-31.8	-28.2	-3.6
	6	-17.3	-22.4	5.1
	10	-12.2	-21.6	9.4
∞	1	-18.2	-15.5	-2.7
	3	-16.7	-16.3	-0.4
	6	-14.4	-19.0	4.6
	10	-14.3	-21.7	7.4

3.4 Discussion of choice of investigated cases

The amount of possible cases that could be investigated is vast as propellers may in themselves vary in length, shape and material, and the used radar waveform may be varied in polarisation, elevation angle and carrier frequency. Therefore, these different properties or parameters are in Section 3.2 varied individually with other parameters held fixed.

A base case is defined as a propeller of length 23 cm, pitch 4.7” and ε_r=8.0 with a radar waveform with HH-polarisation, elevation angle θ=90° and carrier frequencies f={1; 3; 6; 10} GHz. This is chosen since the length and pitch are typical for the kind of multicopters of interest in this study. HH-polarisation is seen to yield much higher RCS values, thus it is of greater interest than VV-polarisation in radar detection of these targets. The dielectric constant is chosen since high values of this may be observed as carbon fibre is highly reflective. From this base case, all the investigated cases originate and each case with their varied parameters is shown in Tab. 3-4. It is evident from this table that many more variations could be performed, e.g. change in polarisation for another ε_r. Although, by holding most

parameters fixed while varying a single parameter as has been done here gives indications of trends in the dependence on the varied parameter.

One parameter that is not varied in this study is the pitch or shape of the propeller. This likely has an impact on the results at 10 GHz where the structure of the propeller is more impactful. This is however left for future studies to investigate.

Tab. 3-4. A summary of the investigated cases. As is evident from this, there are many combinations of parameters that have not been investigated. Although, the same trends shown in the investigated cases may be applicable to other variations as well.

Case name	ε_r	**Length [cm]**	**Polarisation**	**Elevation angle [°]**	**Frequency [GHz]**
Polarisation	8.0	23	HH, VV	90	10
Dielectric constant and frequency	2.0, 3.4, 5.7, 8.0, ∞	23	HH	90	1, 3, 6, 10
Frequency sensitivity	8.0	23	HH	90	1.1, 3.3, 6.6, 10.5, 11
Elevation	8.0	23	HH, VV	50, 70, 90, 110, 130	6, 10
Length	8.0	23, 25.5, 28	HH	90	1, 3, 6, 10

4 SIMULATION OF MULTICOPTER AND DISCRIMINATION FROM BIRDS

The previously calculated static electromagnetic response of a propeller is in this chapter used to simulate a full multicopter in motion. Using a quasi-static approach, the complex-valued electric field response of the propeller is rotated and the far field can be analysed in the time domain.

Several aspects of dynamic simulation are considered. Firstly, the use of ISAR techniques on the propeller is analysed to see whether it is possible to characterise it in this way. Then the micro-Doppler spectra for different frequencies and materials are generated and discussed. Thereafter, the use of SVD for extracting information from the micro-Doppler signatures is analysed and, lastly, the expected radar return of birds is discussed in comparison to the simulation results of the multicopter radar return.

4.1 Dynamic simulations using Matlab

The calculated static radar return of a propeller is imported in the computational software Matlab for further analysis. Dynamic simulations are then performed where rotation of the propeller is simulated by rotating the complex-valued electric far field at some angular velocity ω and storing the received field at each time step, creating a continuous time signal. If the received field is denoted $\overrightarrow{E_s}$, the rotation of the complex-valued electric far-field may be expressed as

$$\overrightarrow{E_s}(\varphi_i) = \{\varphi_i = \omega t\} = \overrightarrow{E_s}(\omega t) \Rightarrow RCS(\varphi_i), \tag{4.1}$$

where φ_i is the azimuth angle at a time step i.

This is a form of quasi-static motion as the movement is approximated as many static instances in succession, sampled at a certain sample rate. Bandwidth effects from the pulse width in pulsed Doppler radars are not considered and, thus, this analysis is not exclusively applicable for these systems. However, the PRF of pulsed Doppler systems may be seen as the sample rate of a signal and therefore this type of continuous wave analysis, without explicit pulse generation and bandwidth effects, is still accurate for this system.

To perform the STFT analysis and create the joint time-frequency micro-Doppler spectrum, the function *spectrogram(...)* is used. It performs a number of STFTs in succession and joins them with overlaps to form a spectrum. In this function, different parameters can be set such as the type of window function used to define the limits of each STFT, the amount of samples that overlap between two consecutive STFTs and sample frequency used. The window function is set to the default hamming window for the calculations herein. The overlap of STFTs affects the appearance of the spectrum. It has been shown that the amount of overlap needed for resolving multicopter spectrums is about 70-85%. For a smooth spectrogram of birds, a higher overlap of 90-95% is needed [9]. Thus, an overlap of 90% is used in these simulations.

The range- and cross-range profiles are created through taking the inverse Fourier transform of the signal as the propeller is observed from φ=-90° to φ=90°. However, the amount of samples in this set is quite low and the result is a coarse point scatter distribution. To counteract this, zero padding is used, which is a technique used to get more frequency bins in a Fourier transform by adding zeros to the end of a dataset before taking the transform.

4.2 Multicopter model

The multicopter is modeled as several propellers being independent of each other. This implies that interaction between propellers such as multiple bounces of the electromagnetic radiation is not considered, which is a reasonable assumption as long as the propellers are separated at a far enough distance apart. The propellers are given individual rotational rates and starting angles. Also, the rotational rates are set to deviate somewhat from each other as the propellers in hover operation in a real scenario are generally not at the same speed in order to compensate for the turbulent air. Furthermore, the model used herein does not take into account the small change in rotation rate over time of each propeller which is occurring in a real scenario to stabilise the vehicle.

The multicopter body or fuselage is not part of this model. Thus, multiple bounces or other wave phenomena from the interaction with the body are not considered. The body produces a rather strong radar return in comparison to the smaller propellers. However, the Doppler shift of the body is much smaller and thus the propellers are distinguished by their micro-Doppler spectra. In simulations, the multicopter is set to be stationary or hovering, i.e. the main velocity component is zero. The main velocity is generally much smaller than the rotational speeds of the propellers, in the order of 10 m/s and therefore only slightly moves the spectra along the Doppler frequency axis.

4.3 Range and cross-range profiling

The range- and cross-range profiles of a single propeller are created using the Matlab function *ifft(…)* which uses the inverse fast Fourier transform (IFFT), which is a computationally efficient way of calculating the IFT. The complex-valued electric field is taken at angles $-90° \leq \varphi \leq 90°$ with a resolution of 1°. However, as seen in (2.17) the Fourier relationship is between $\sin(\varphi)$ and y_i, therefore the data points must be evenly spaced in $\sin(\varphi)$ instead of φ for the IFT to give a correct profile. The data is thus firstly interpolated linearly to angles φ_{new} such that $-1 \leq \sin(\varphi_{new}) \leq 1$ where the difference between any neighbouring two angles $\varphi_{new,n}$ and $\varphi_{new,n+1}$ fulfil $\sin(\varphi_{new,n+1})-\sin(\varphi_{new,n})$=constant. To enhance the resolution in the IFT, zero padding is used and is set to a sufficiently high value where the solution does not change much with increased padding. The resulting IFT must also be rescaled with the factor k/π originating from the variable substitution.

The cross-range profile is constructed using the radar return at different frequencies and the result is shown in Fig. 4-1. The dielectric constant chosen in this case is ε_r=3.4. It is seen that the propeller length of 23 cm is matching the width of the solutions of the higher frequencies 3, 6 and 10 GHz, while 1 GHz predicts the length more poorly. The point-scatter model used in this analysis is mostly valid at high frequencies and this is obvious from the 10 GHz case, where much more detail in the point-scatter distribution is revealed. The deep and narrow

minima of the 10 GHz cross-range profile are a consequence of going from a finite-element model used in the static calculations, to a point-scatter model in the IFT which is not considering complicated wave phenomena. Another factor may be that the zero padding used introduces data points which are not resolved by the original data which is collected with a 1° resolution. Cross-range profiles are also examined at different lengths and dielectric constants to see whether this would have any effect on the profile. In Fig. 4-2a), it is seen that the dielectric constant affects the amplitudes of point scatterers, while the width remains constant. The length is varied in Fig. 4-2b) where the width is seen to be in good agreement with propeller length.

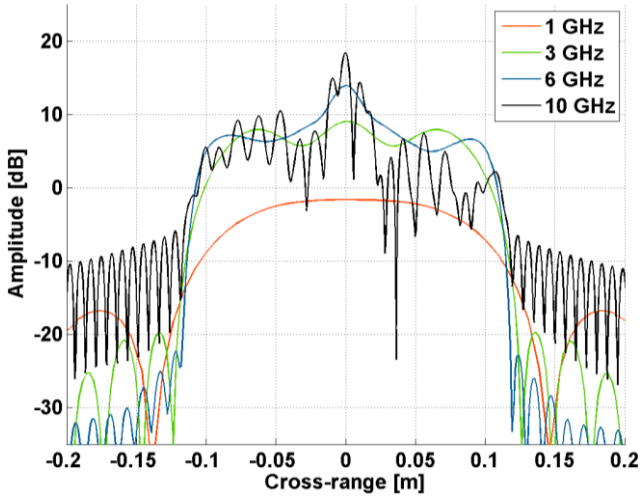

Fig. 4-1. Cross-range profile for frequency variation with ε_r=3.4. The propeller length of 23 cm matches the width of 3, 6 and 10 GHz while 1 GHz predicts it more poorly.

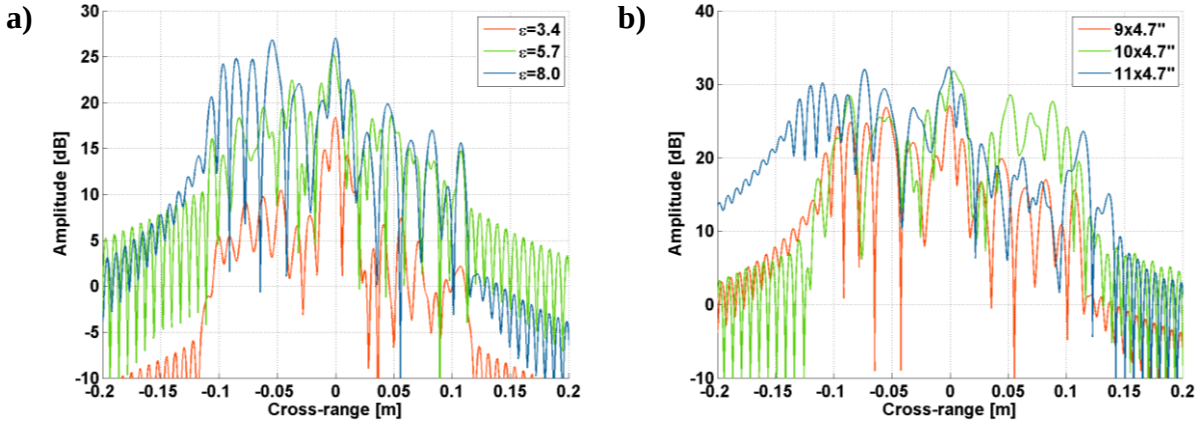

Fig. 4-2. Cross-range profile at f=10 GHz. **a)** ε_r is varied for a 23 cm propeller. The width of the IFT is constant and predicts the length. **b)** Length is varied with ε_r=8.0. The widths of the IFTs are 22.3 cm, 24.8 cm and 27.8 cm which follow the tested lengths.

Range profiles are created by extracting the phase from the IFT and dividing by 2k. As the point scatter distribution model is a high frequency scattering model, it is evaluated at 10 GHz for different dielectric constants as seen in Fig. 4-3. The low dielectric constant of ε_r=2.0 is also used. All curves are moved to origin in order to better reveal their internal structure. For

ε_r={2.0; 3.4} a sinusoidal curve is seen with a range distance amplitude of ±1 cm which corresponds to the width of the propeller. This suggests that the point scatterers along the propeller may be resolved in range as well using this method, revealing the sinusoidal shape of the object. However, looking at the results of the other dielectric constants, it is clear that the shape of the curves differs by quite a lot, even though the geometry of the object remains the same. That this type of analysis would work at a low dielectric constant and not at high could be due to the large end-fire lobes being comparable or even larger than the broadside lobe at high ε_r while they are smaller than broadside at low ε_r. The large end-fire lobes are not predicted by the point-scatter distribution model used in deriving this range profile and could therefore affect the solution. This however, needs to be further investigated.

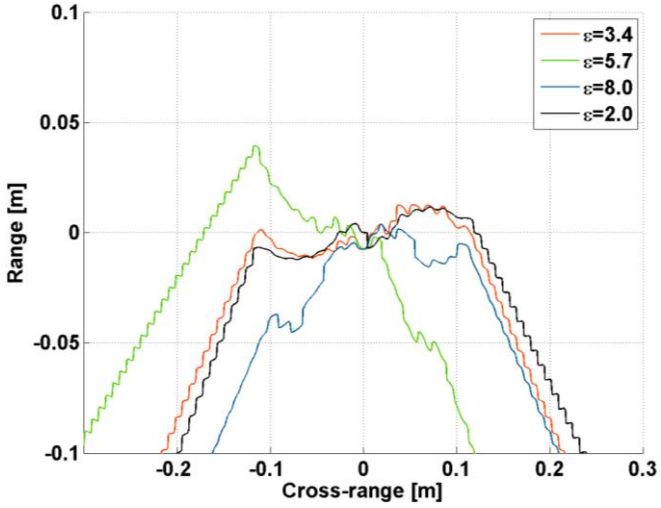

Fig. 4-3. Range profiles calculated for different ε_r. ε_r=3.4 and ε_r=2.0 show sinusoidal curves with amplitudes ±1 cm which correspond to the width of the propeller. However, other values of ε_r do not predict this as well.

4.4 Micro-Doppler signature

The complex-valued radar return for the 23 cm propeller is rotated multiple revolutions at a given rotation rate in order to generate a micro-Doppler spectrum. If the received signal is the sum of the contribution from many moving point scatterers, the total received signal can be expressed as

$$S = \sum_{i=1}^{P} a_i e^{j2\pi(f+f_{D,i})t} = \sum_{i=1}^{P} a_i e^{j\varphi(t)}\, e^{j2\pi f t}, \tag{4.2}$$

where P is the total number of scatter centres, a_i is the amplitude of scatterer i, $f_{D,i}$ is the time varying Doppler shift in radial direction from the radar caused by scatterer i and $\varphi(t)=2\pi f_{D,i}t$. In the second step, the field has been written in terms of a varying phase and a periodic function. The first exponential term, $a_i e^{j\varphi(t)}$, is the phasor which has amplitude and phase information about the signal. As HFSS calculates the far-field, the result is presented with a phasor without the time-varying signal, thus the signal received as the propeller is rotated in Matlab is

$$S = \sum_{i=1}^{P} a_i e^{j\varphi(t)} = \sum_{i=1}^{P} a_i e^{j2\pi f_{D,i} t} \tag{4.3}$$

and calculating the STFTs of this signal generates a frequency spectrum of the Doppler shifts rather than the true frequency of the signal which is $f+f_{D,i}$. The Matlab script used to generate the micro-Doppler spectra can be seen in Appendix D.

4.4.1 Single propeller

The micro-Doppler spectrum is first simulated for a single propeller. The rotation rate is set to f_{rot}=125 Hz (corresponding to 7500 RPM) which gives a time period of T=8 ms per full revolution and a tip velocity of v_{tip}=90 m/s. This rotation rate is what could be expected from larger sized propellers, whereas smaller ones would most likely rotate at a much higher rate.

The simulation is carried out for the calculated radar returns at 10 GHz for the different dielectric constants ε_r={2.0; 3.4; 5.7; 8.0; ∞} in order to see how the large end-fire lobes may impact on the signatures. The results of this variation are shown in Fig. 4-4. All spectra show the expected time period of 8 ms. The Doppler shift of the tip at this frequency, calculated using (2.2), is $f_D \approx 6.0$ kHz which also matches the amplitudes of the spectra. For ε_r={2.0; 3.4} the spectra are less chaotic, whereas for ε_r={5.7; 8.0; ∞} the spectra are more difficult to interpret. This is in correlation to their individual, static radiation patterns as the end-fire lobes are slightly lower than broadside lobes at lower ε_r and at higher ε_r the end-fire lobes cause stronger signal at $f_D \approx 0$. The PRF is here chosen as 15 kHz to be able to resolve the Doppler shift of the tip and also show distinction from the background.

Micro-Doppler spectra are also simulated at different carrier frequencies and the results of this are presented in Fig. 4-5 where ε_r=3.4 was used and the same f_{rot} and PRF as previously. The width of the spectra matches calculated Doppler shifts of the tip at the different frequencies, which are f_D={6.0; 3.6; 1.8; 0.6} kHz for carrier frequencies 10, 6, 3 and 1 GHz respectively. The sometimes occurring straight lines in the figures are due to an aliasing effect originating from the Fourier transforms and as they are much smaller than the main part of the spectrum they are considered part of the background noise.

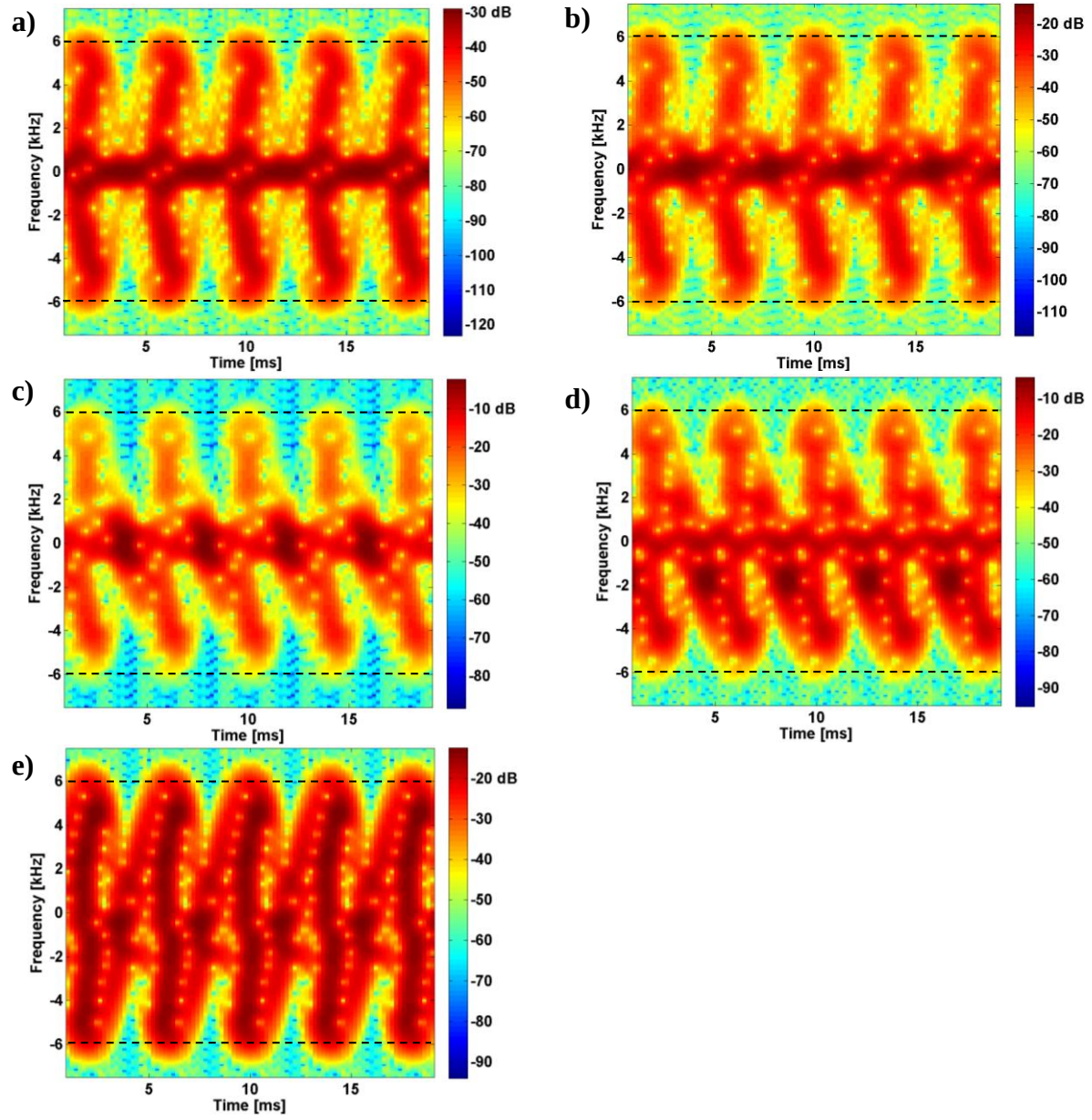

Fig. 4-4. Micro-Doppler spectra at f=10 GHz for different dielectric constants: **a)** 2.0; **b)** 3.4; **c)** 5.7; **d)** 8.0; and **e)** ∞. The theoretical Doppler shift of the tip at this frequency is indicated as dashed lines. Note the different scales in amplitude as they are chosen to emphasize relative difference within each figure.

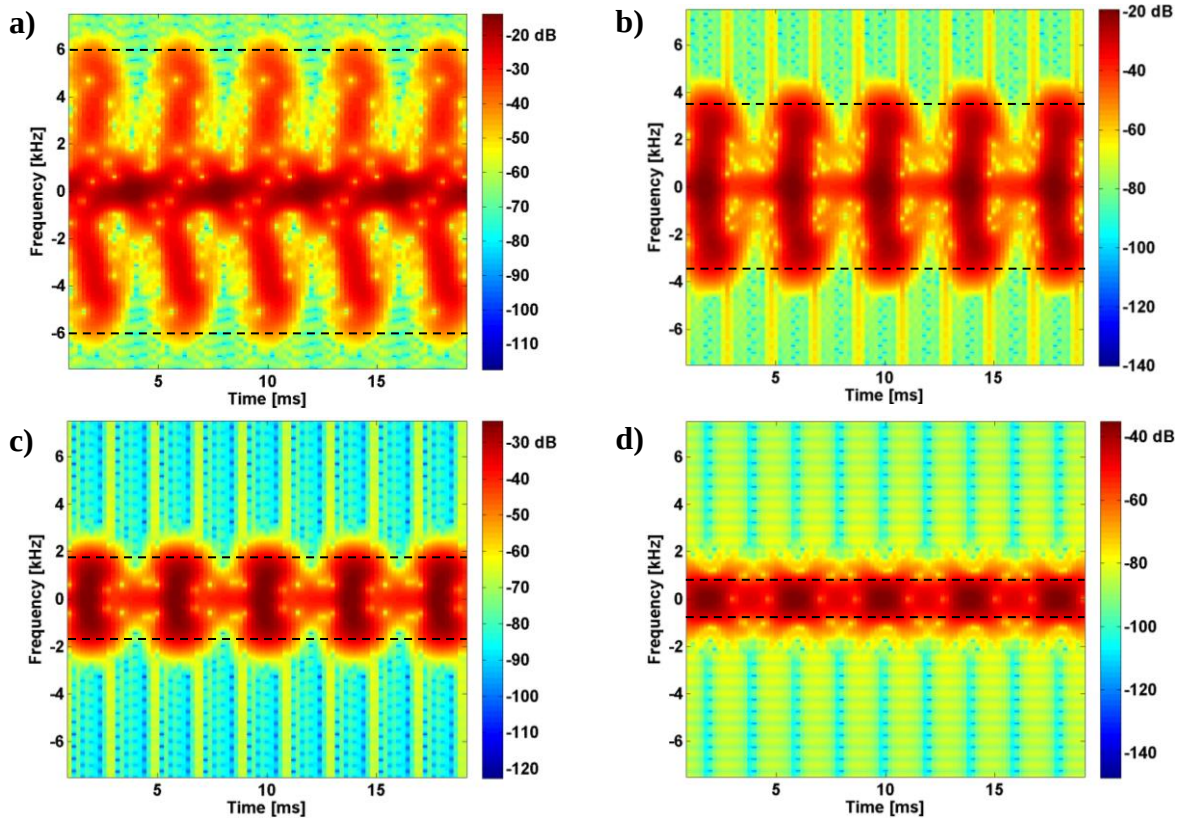

Fig. 4-5. Micro-Doppler spectra for ε_r=3.4 for different carrier frequencies: **a)** 10 GHz; **b)** 6 GHz; **c)** 3 GHz; and **d)** 1 GHz. Dashed lines indicate the theoretical Doppler shift of the tip at that carrier frequency. Note the different scales in amplitude as they are chosen to emphasize relative difference within each figure.

4.4.2 Multiple propellers

The simulated radar return of a single propeller is a much more simple case than the radar return expected from a full multicopter. Although, by superimposing the radar return of many propellers at the same time, rotating at different starting positions and rotation rate, the model may come closer to the real scenario.

A simulation using four propellers with ε_r=3.4 is performed. The frequency chosen for this simulation is 10 GHz as it generated a wide and clear spectrum for a single propeller as seen in Fig. 4-5a). Two of the propellers are rotating CW and two are rotating CCW. The radar return for a CW-model propeller is created through mirroring the calculated radar return for the CCW-model. The received signal is then a summation of the electric field from all four propellers at every time instant. Starting angles are set to arbitrary values and rotation rates are set to have a mean of f_{rot}=125 Hz, although with a slight deviation of maximum ±10%. The simulated micro-Doppler spectrum is shown in Fig. 4-6 and it is clearly much more chaotic than the simple, single propeller case. It is very difficult to find any periodicity that relates to a single propeller. The Doppler shift of the tip can however still be distinguished. As the spectrum has a chaotic behaviour for 10 GHz, which yielded a clear spectrum for the single propeller, it is believed to have a similar appearance at the other carrier frequencies.

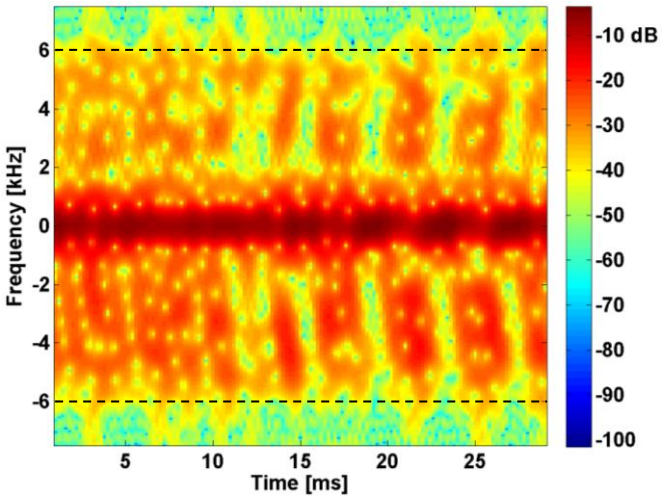

Fig. 4-6. Simulated micro-Doppler spectrum of a four propeller multicopter at f=10 GHz. The Doppler shift of the tip roughly matches the calculated value of f_D=6.0 kHz (dashed lines) corresponding to the mean rotation rate f_{rot}=125 Hz used in this simulation.

4.4.3 Integration time and PRF

Integration time and PRF are important radar design parameters when it comes to detection of a target using its micro-Doppler spectrum. These parameters are here studied for a single propeller of total length L which can later be generalised to multiple propellers. Calculations in this section follow the calculations made in a previous study in [14].

As the largest Doppler shifts occur at broadside, this is where the main characteristics appear and PRF must thus be chosen such that the broadside flash is sampled at every revolution. The rotation rate of the propeller is given by

$$f_{rot} = \frac{v_{tip}}{\pi L} \tag{4.4}$$

Using this along with the expression for the lobe width in (2.9), the duration of the flash can be calculated as the lobe width divided by the angular frequency ω, which then becomes

$$\tau_{flash} = \frac{\Delta\varphi}{\omega} = \frac{\Delta\varphi}{2\pi f_{rot}} = \frac{\frac{\lambda}{2L}}{2\pi\frac{v_{tip}}{\pi L}} = \frac{\lambda}{4v_{tip}} \tag{4.5}$$

To guarantee one complete sample during the broadside flash, the PRI together with the pulse width, τ_{pulse}, must not exceed the time of the flash, τ_{flash} [23]. This sets the requirement on the PRF as

$$PRI + \tau_{pulse} \leq \tau_{flash} \Rightarrow PRF \geq \frac{1}{\tau_{flash} - \tau_{pulse}} \tag{4.6}$$

and if the pulse width is assumed to be much smaller than the flash time, i.e. $\tau_{pulse} \ll \tau_{flash}$, the PRF requirement becomes

$$PRF \gtrsim \frac{1}{\tau_{flash}} = \frac{4v_{tip}}{\lambda} \tag{4.7}$$

This expression may be compared to the PRF required for unambiguous velocity in (2.3) and it is seen that the two expressions are identical for unambiguously sampling a velocity v_{max}=v_{tip}. This has the consequence that if the pulse width is much smaller than the broadside flash time, every broadside flash is sampled with at least one complete pulse as long as the velocity of the tip is unambiguously resolved.

In Tab. 4-1, minimum PRF requirements for different plausible tip velocities and frequencies are tabulated which shows that required PRF may be up to 20 kHz at X-band to detect a tip velocity of v_{tip}=150 m/s. Velocities were chosen to be lower than the speed of sound and to yield reasonable RPMs of 5000 to 11000 for a 10" propeller. The shortest flash times are listed as well since the pulse width must be much shorter than this time for this PRF requirement to be valid. If for example a pulse width of τ_{pulse}=0.1τ_{flash} is used, using (4.6) gives a change in PRF as PRF $\geq \frac{1}{1-0.1}\frac{4v_{tip}}{\lambda}$ which gives a change by +11% to PRF values found in the table. The maximum unambiguous distance R_{max} is also shown for the largest PRF at each frequency.

Tab. 4-1. Minimum PRF needed to resolve three plausible tip velocities at different carrier frequencies. The flash times are listed for the highest tip velocity as the pulse width is assumed to be much smaller than the flash time. Also, unambiguous range is shown for the highest PRF at each frequency. These calculated values follows [14].

Frequency [GHz]	**Minimum PRF requirement [kHz]**			τ_{flash} **[ms]**	R_{max} **[km]**
	v_{tip}**=70 m/s**	v_{tip}**=100 m/s**	v_{tip}**=150 m/s**	v_{tip}**=150 m/s**	v_{tip}**=150 m/s**
1	0.9	1.3	2.0	0.500	74.9
3	2.8	4.0	6.0	0.167	25.0
6	5.6	8.0	12.0	0.083	12.5
10	9.3	13.3	20.0	0.050	7.5

The integration time needed to accurately classify a target is more difficult to determine. The time needed to guarantee detection of at least one flash is to illuminate the target over the course of half a revolution of the propeller. This time is expressed as

$$\tau_{int} \geq \frac{1}{2f_{rot}} = \frac{\pi L}{2v_{tip}} \tag{4.8}$$

Using this integration time, the full width of the Doppler shift in the joint time-frequency spectrum is captured in the time span and detection methods which only rely on the tip velocity could be used. Although, this is not robust as flashes may be missed due to missing data points. Also, periodicity is not found when only one flash has been sampled. In order to extract any periodicity, two flashes or more are needed, thus τ_{int} needs to be at least twice as long as in (4.8), i.e.

$$\tau_{int} \geq \frac{\pi L}{v_{tip}}. \tag{4.9}$$

It is seen in (4.9) that the integration time is only dependent on the properties of the propeller and independent of the radar frequency.

Tab. 4-2 shows minimum integration times for detecting periodicity in the micro-Doppler spectrum for different tip velocities and propeller lengths. Although, longer times are most likely needed for robust detection as many periods are needed to build confidence of correct classification. It should also be mentioned that calculations have been carried out for a single propeller. By definition, multicopters use more than one propeller, thus the time to detect one broadside flash decreases significantly.

Tab. 4-2. Minimum integration time needed for different propeller lengths and tip velocities based on time for one revolution. Lengths of 60-80 cm are more likely for small helicopter UAV rather than multicopter.

Propeller length [cm]	**Minimum integration time [ms]**		
	v_{tip}=70 m/s	**v_{tip}=100 m/s**	**v_{tip}=150 m/s**
20	9.0	6.3	4.2
40	18.0	12.6	8.4
60	26.9	18.8	12.6
80	35.9	25.1	16.8
100	44.9	31.4	20.9

Another parameter that may be changed is the time interval on which the Fourier transforms are taken. With a long integration time of the target, a long time can be used in the STFT, which then may reveal the Doppler shift of the overall rotation rate of the propeller on this interval instead of the instantaneous Doppler shifts. This is simulated and illustrated in Fig. 4-7 where the two previously examined cases of one and four propellers are examined with short and long times in the STFTs. In the case of one propeller, the longer time interval reveals the rotation rate through the difference between two neighbouring lines in the spectrum. This difference is double the rotation rate as there are two flashes in the micro-Doppler spectrum per revolution. The width of the spectrum also corresponds to the Doppler shift of the tip. In the case of four propellers, the longer time interval performs more poorly as the difference between lines is no longer as constant. However, the width does still correspond to the Doppler shift of the tip.

4.5 Using SVD for detection algorithms

If the micro-Doppler signature of multicopters is to be used in a radar system application, there needs to be a way of extracting information from the spectrum in order to classify the target using classification algorithms. As was seen previously in Section 4.4.2, the signature is expected to be quite chaotic in its overall behaviour as the number of propellers on the UAV increases, thus extracting useful information is not an easy task to do. One way to do this however, is with the use of SVD.

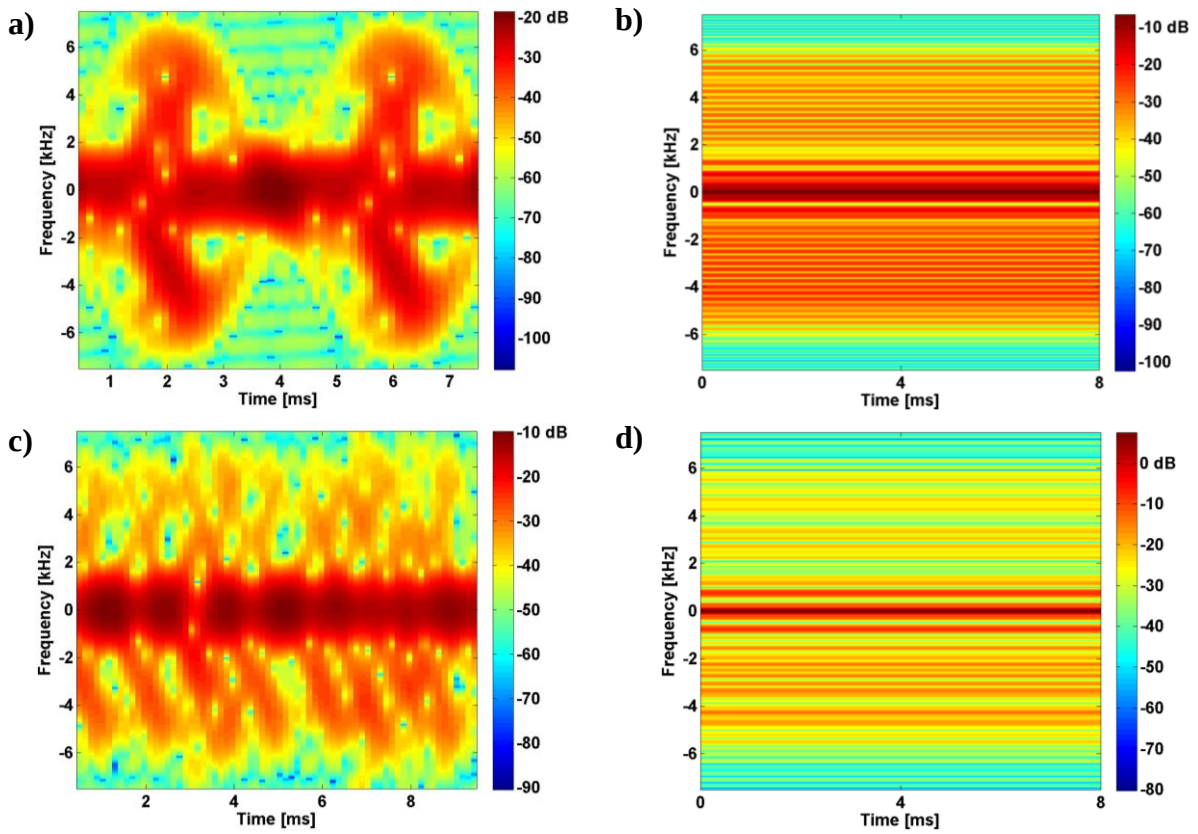

Fig. 4-7. Comparison of STFTs applied to long and short time intervals. **a)** and **c)** show the short time intervals for STFTs for a single propeller and four propellers rotating at mean rate f_{rot}=125 Hz. **b)** and **d)** show the long time intervals for the same simulations. For the single propeller, long STFT reveals the rotation rate as the distance between lines is mostly $2f_{rot}$=250 Hz whereas the four propeller case does not reveal correct rotation rate as the lines are seen to be more arbitrarily spaced out.

SVD is applied to the same signal seen in Fig. 4-6, generating three matrices Σ, U and V. There is a Matlab function for performing this operation called *svd(…)* and the data fed to this function is the complex field data after the STFTs have been performed. A relatively long time of 50 ms is used as integration time to get a clear micro-Doppler signature of the target. Fig. 4-8 shows the SVD analysis of the tested signal. The first 10 singular values of Σ are shown and it is clear that the first value is much larger than the others. This value is coupled to the strongest signal, which is the signal around Doppler frequency, f_D=0. When analysing the first three vectors in the U matrix, it is seen that the first vector matches the width of the 0 Doppler frequency signal. The second and third vectors on the other hand better matches the width of the entire spectrum which is approximately between f_D=-6 kHz and f_D=6 kHz. The periodicity of the signature is analysed with the V-vector in which distinct peaks can be seen. Using the time between two distinct peaks chosen as marked in the figure and taking this as the time for half of a revolution, as two flashes in the micro-Doppler signature is expected per revolution, the rotation rate of f_{rot}=125 Hz is obtained which is the mean rotation rate of the propellers.

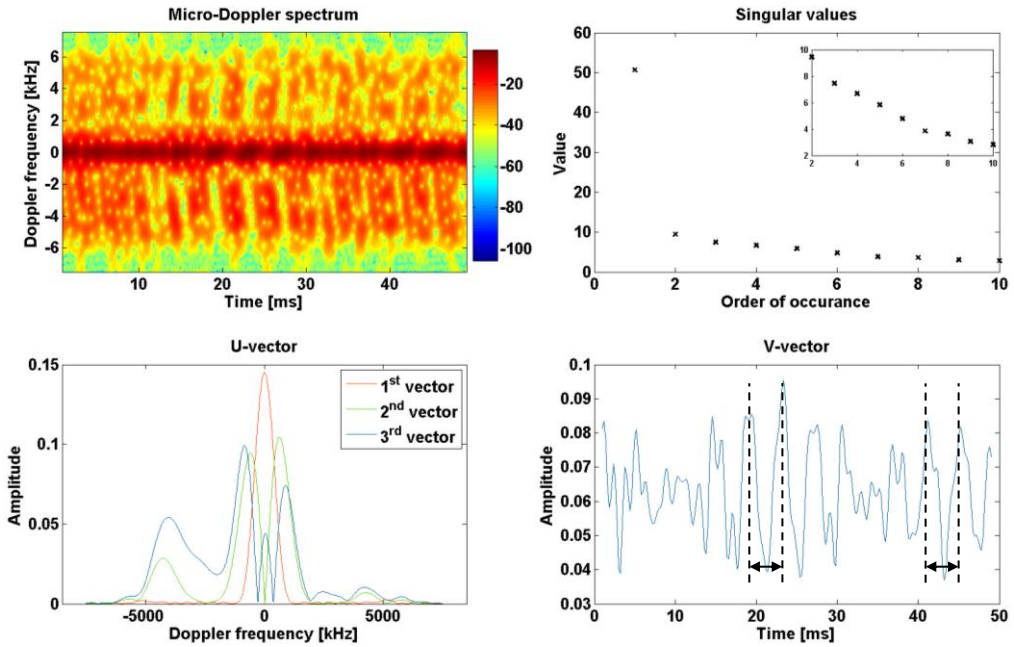

Fig. 4-8. SVD analysis on four 23 cm propellers with mean rotation rate f_{rot}=125 Hz. The first three U-vectors, corresponding to the three largest singular values, are plotted, of which the 2nd and 3rd vector couple quite good to the width of the Doppler shifts. A clear periodicity is seen in the first V-vector which reveals a rotation rate of nearly 125 Hz when measured between marked peaks. The 10 first singular values are shown; however, as the first singular value is much larger than the others, the inset shows the following 9 singular values.

This shows that SVD may be used as a simple, yet effective technique of extracting two main features from a micro-Doppler signature: width of the spectrum and the periodicity of the spectrum. If both the width and the periodicity can be accurately determined, the length of the propeller may be calculated from using (4.4) and instead solve for *L*. This information is important when the classification system not only distinguishes multicopters from birds, but also categorises different multicopters from their propeller lengths. As previously mentioned in Section 1.3, SVD in combination with machine learning algorithms has been successfully used in classification of multicopter UAVs [7]. However, the use of algorithms to extract information from the SVD analysis has not been thoroughly studied in this thesis.

4.6 Radar return of birds and bird discrimination

The radar return of birds has been investigated previously in a number of studies. As mentioned earlier, the wing beat frequency of birds is expected to be up to 20 Hz which is much lower than the rotation rate of a multicopter propeller of 125 Hz used in this report. The translational air speed of birds is on average 14.3 m/s but some species regularly exceed 20 m/s where faster birds often correlate to larger sized birds [20]. The tip velocity of a bird wing, including the translational velocity of the whole body, is believed to stay below 25 m/s in most cases [8]. These properties of bird flight behaviour suggests that a long integration time is needed to sample the slow wing beat period and that a lower sample rate is sufficient to sample the lower Doppler shifts to create the micro-Doppler signature. These criteria are the opposite of what has been seen for multicopter UAV detection where a high sample rate and a shorter integration time are needed.

An example of a measured micro-Doppler signature of a large sea bird with a wing length of approximately 80 cm can be seen in Fig. 4-9 which is a reproduced image from [4]. The used radar uses VV-polarisation and operates at X-band. The bird is seen both at broadside and from head-on and the translational velocity has been removed. There is a clear difference in the width of the Doppler shifts where broadside illumination gives a much smaller width, even though the bird is flapping its wings during the entire time interval. From the head-on micro-Doppler signature it is evident that the tip velocity is much lower than that of multicopter UAVs as it is around 4 m/s relative to the body of the bird. This makes distinction between the two classes feasible as the Doppler shifts of birds would be at around 250 Hz at 10 GHz radar frequency in comparison to 6 kHz of a rotating propeller. This implies that if the PRF is optimised towards multicopter detection, birds are also seen as a narrower spectrum width. Although, a positive classification of birds would require a longer integration time of up to 0.5 s to capture the periodicity of the motion assuming a worst case scenario of 2 Hz wing beat frequency.

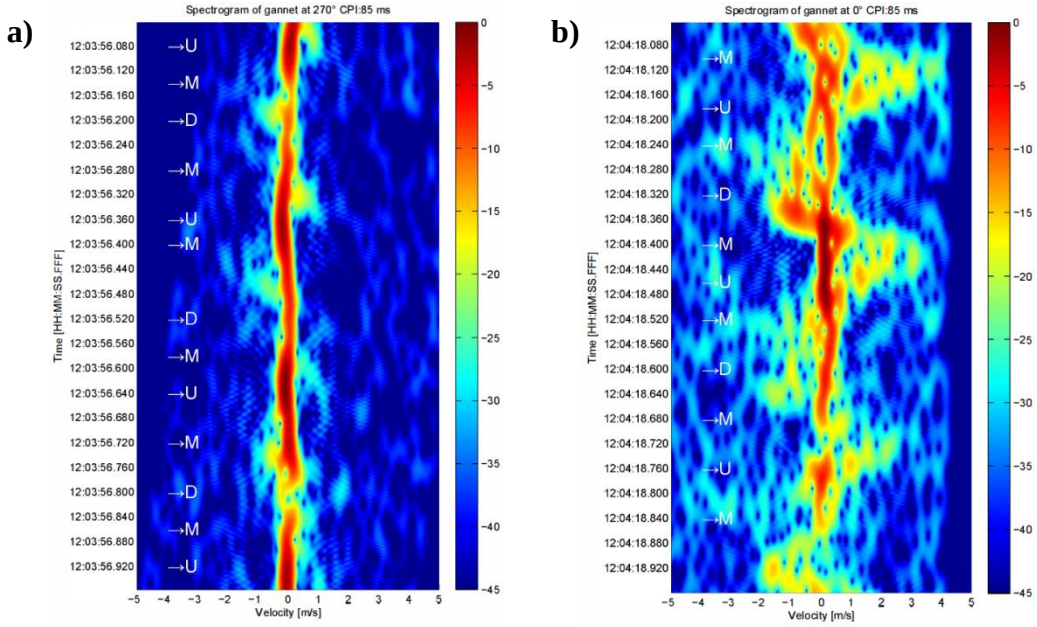

Fig. 4-9. Measured micro-Doppler signature of a large sea bird seen at: **a)** broadside; and **b)** head-on. The used radar is vertically polarised and operates at X-band. Wing beats are hardly seen at broadside and are more prominent at head-on. The letters show position of the wing in its cycle where U=up, M=middle and D=down. From [4], © 2014 IEEE. Reproduced with permission.

5 RESULTS AND DISCUSSION

In previous chapters, the radar return of multicopters has been simulated and compared to that of birds and expressions of how to describe this radar return have been presented. These results are in this chapter summarised and discussed in order to choose radar design parameters for better detection of multicopters. Furthermore, an analysis of the errors present in this study is performed, followed by a broader perspective on the societal consequences of the study as well as suggested continued work in this field.

5.1 Choice of radar design parameters

In designing a radar system for detection of multicopters and discriminating them from birds, there are several design parameters that may be changed which affect detection. These parameters are mainly: polarisation, carrier frequency, PRF, pulse width and integration time.

The polarisation of the radar waveform was shown to have great impact on the amplitude of the RCS of a propeller. VV-polarisation was approximately 17.2 dB lower than HH-polarisation at broadside for ε_r=8.0. This means that HH-polarisation would be the better choice of the two when it comes to this kind of detection.

It has been shown that the RCS of a 23 cm propeller varies quite a lot for different radar frequency bands. The 10 GHz carrier frequency gives a complicated behaviour, showing four large RCS flashes per revolution whereas 1, 3 and 6 GHz only show two flashes. Although, all four flashes do not appear in a micro-Doppler signature as the large RCS at end-fire does not give high Doppler shifts as the propeller is moving perpendicular to the radar at that time, thus a periodicity is still observed. The choice of carrier frequency more importantly affects the broadside lobe width, where the largest Doppler shifts occur. This lobe width is seen as inversely proportional to frequency, thus a higher frequency results in shorter broadside flashes. It also affects the maximum Doppler shift detected for a fixed tip velocity. Thus a wider micro-Doppler signature is seen at higher frequencies making the Doppler shifts of the propeller tips more easily distinguishable from the Doppler shift of the fuselage. Furthermore, higher amplitude of the broadside RCS is shown at 6 and 10 GHz as compared to 1 and 3 GHz. There is however not much difference between 6 and 10 GHz in this amplitude. Without taking any other parameter into consideration, this overall suggests that a higher frequency band is preferable as long as the smaller lobe width of the broadside flash can be sufficiently sampled.

To sample the broadside flash, the pulse width and PRF must be considered. It was shown that a PRF of 20 kHz is necessary to resolve a tip velocity of 150 m/s at X-band, whereas 12.0 kHz was needed at C-band for the same case. These PRFs were also shown to resolve the tip velocity unambiguously, as long as the pulse width was chosen such that it became very small in comparison to the flash time. Flash times may be very short at this tip velocity, thus the pulse width must be in the order of 8 or 5 μs if it is chosen as 1/10 of the flash times seen in Tab. 4-1 at C- or X-band to resolve 150 m/s.

The last radar design parameter that needs to be considered is the integration time. This parameter is chosen such that a target may be found and classified by classification

algorithms. This is independent of the radar frequency and depends on the properties of the propeller. Furthermore, the efficiency of the classifier is an important factor and developing automatic classification is not part of the scope of this study. Thus an integration time is difficult to set. It is however likely that at least one flash needs to be observed to see the full width of the micro-Doppler signature from a multicopter. It is also likely that if any classification based on periodicity in the signature, where different multicopters are distinguished and classified on the basis of their propeller length, is to be used, at least a full period of the propeller, i.e. two flashes, need to be sampled. Times would then be up to 20 ms for multicopters with slowly rotating propellers or up to 50 ms for small helicopter UAV. However, if birds are to be positively classified, an even longer time of up to 500 ms is necessary to capture their periodic nature. Of course, a longer integration time is always beneficial for UAV classification as well since many periods of the signature only makes classification more robust. The problem with a longer integration time though is that the time schedule of a search and track radar must be very fast in order to not let targets move too far in between detections, thus long times are seldom afforded. One way to shorten the integration time could be to only positively classify multicopters and say that anything else in the air which does not generate high Doppler shifts is most likely a bird and may be disregarded.

In summary from this discussion, good detection using a monostatic, pulsed Doppler radar is achieved using HH-polarisation, high carrier frequency, high PRF, narrow pulse width and a long integration time.

5.2 Error analysis

It is important to emphasize that this study has used a computational approach to the problem. The computations have discretised phenomena which are continuous in the real world and conditions have been assumed perfect, without any background noise. Even though adaptive meshing has used a discretization which ensures a good approximation of the continuous case, real measurements could be performed to confirm this kind of computations. Although, the benefit with using computations is that not everything needs to be measured as a good idea has been developed as to what should be the optimal setup.

Another error occurring in the simulated environment is due to the CAD model being used. Electromagnetic computations are very sensitive to the quality of the 3D structure as very tiny cavities or tiny gaps in between surfaces may cause resonances of an incoming electric field, thus having a large impact on the overall result. Sharp edges of a CAD model are also especially hard for HFSS to mesh as this is a complicated area in terms of electromagnetic interaction and the model used for the propeller has many sharp edges. A consequence of the meshing of the sharp edges may in some cases be seen in the RCS at ±90° as a small, unsmooth discontinuity or jump from one value to the next. This is not expected as the RCS at 90° should equal that at -90° for symmetry reasons. This discontinuity was however hardly noticeable in most cases but in some it was more prominent, e.g. in the 6 GHz calculation in Fig. 3-7c) where the discontinuity is 0.8 dB.

5.3 Societal consequences

Studies within the field of detection systems for multicopter UAVs would in the end hopefully lead to an increased security in our society as they provide means of dealing with UAVs which are disrupting order or are in some way hostile. There are however secondary effects that may originate from this kind of work and that one should be aware of going forward. For example, this study gives insights into detection with the intent to be used for optimising system design parameters. On the other hand, the same insights could be used by those who want to conceal their UAVs as the insights also indicate when the system is flawed and not performing as well. A direct example of this would be the use of ducts which has been shown to hide the propellers for highly reflecting materials or the use of propellers made of a material with a low dielectric constant.

Another issue is how to deal with a hostile UAV once it has been detected and deemed hostile. Simply neutralizing it in the air would in crowded areas mean that it could fall onto someone with lethal force. Methods such as forced take-over of the control of the UAV, jamming controls forcing it to engage auto-land mode or in some way catching it in the air would probably be preferred in these scenarios. Even though this issue needs to be solved, a robust detection is a necessary first step towards this type of defensive system.

5.4 Continued work

This work is an initial, theoretical study of the subject and there is much left that could be done in the field. It would for example be interesting to compare the models in this study with measured data of multicopters and birds in flight using long integration times and high PRF. In general, mathematical models and real measurements seldom coincide perfectly and it would be interesting to see how good the predictions are.

Dielectric constants in this study were chosen with inspiration from measured values at lower frequencies for relevant propeller materials. They can however not be said to be representative at the investigated frequencies, thus RCS measurements, e.g. in an anechoic chamber, of common propellers could be performed to get a more accurate radiation pattern. Alternatively, direct measurements of the dielectric constant for propeller materials at relevant frequencies could be performed.

In the calculations of the static radar return, many cases were covered in this study. However, there are still calculations that may be of interest to perform. One example is that the shape of the propeller was not changed, thus varying the pitch of the propeller could be interesting at higher frequencies where geometry is more impactful.

Detection algorithms constitute a large part of the detection and are an important area in need of investigation. As has been mentioned previously, machine learning algorithms have been successfully used in combination with SVD [7]. One could also think of methods which do not rely on micro-Doppler spectra. One such method is to use a parametric method which detects the fundamental frequencies of a time-varying signal through correlating peaks in the received signal. Another method of extracting information from a signal that has gotten more attention within signal processing in recent years is compressed sensing. This technique takes

advantage of the sparsity of a signal to reconstruct information and in a radar system this could allow a much sparser sample rate which could allow for shorter integration times.

6 CONCLUSIONS

In this thesis, the radar return of multicopters has been modelled for a variety of property changes. The focus lied on the propeller as it is the main contributor to the micro-Doppler signature of the UAV, thus the radar return of the vehicle was approximated as the superposition of the radar returns of its individual propellers.

As frequency and dielectric constant were varied, it was seen that the radiation pattern differs quite a lot between frequency bands, where large end-fire lobes appeared at 10 GHz that were not observed at any of the lower frequencies. This has the consequence that at 10 GHz, four flashes are seen per full revolution of the propeller instead of two which is common in e.g. detection of large helicopter rotor blades. Furthermore, the elevation angle and propeller length were varied. Simple mathematical models predicting characteristics in the RCS were then compared to all the calculated values and it was seen that the broadside lobe width is in good agreement with the model with only a few degrees deviation at higher frequencies. At 1 GHz, the model performed poorly which is attributed to the propeller being 0.76λ at this frequency, thus its electromagnetic response is much like that of a half-wave dipole antenna. The theoretical RCS of a cylinder of a dielectric material was used as an approximation of the amplitude of the broadside RCS. This was seen to overestimate the RCS at higher frequencies and slightly underestimate RCS at lower frequencies, which shows that this model may be used to give a rough estimate of the amplitude at 1, 3 and 6 GHz within a few dB.

The complex-valued radar return was then used to perform range- and cross-range profiles of the propeller for different dielectric constants, frequencies and propeller lengths. Cross-range profiling performed well, predicting the length by the spectrum width of the IFT. A hypothesis was that range profiling could be done by extracting the phase of the result of the IFT. This was however seen to be less successful for all dielectric constants and this may be due to the end-fire lobes not being accounted for in the point-scatter model used.

Micro-Doppler signatures were generated at different frequencies, dielectric constants and number of propellers and it was seen that the four flashes in RCS are not reflected by the micro-Doppler signature as flashes on end-fire give very low Doppler shifts. Mathematical expressions of the minimum requirement of PRF and integration time were presented and it was shown that if the pulse width is much smaller than the time of a broadside flash, each broadside flash is sampled as long as the PRF is chosen such that the tip velocity is unambiguously resolved.

Algorithms extracting features from the micro-Doppler signatures need to be further investigated in the future. One such method could be based on SVD, as briefly analysed herein which could find the width of the spectrum as well as the periodicity by a rather straightforward technique. Other signal processing methods such as compressed sensing or parametric methods also show great potential. As multicopters have much higher velocities of the propellers in comparison to the velocity of the wing tips of birds, it is very plausible that algorithms may be developed that are able to distinguish the two different spectrum widths and discriminate these two target classes. Although, detection may require a rather long integration time in order to capture the behaviour of both multicopters and birds.

BIBLIOGRAPHY

[1] A. Glinz, “Hexacopter Multicopter DJI-S800 on-air,” via Wikimedia Commons, 25 August 2013. [Online]. Available: https://commons.wikimedia.org/wiki/File:Hexacopter_Multicopter_DJI-S800_on-air_credit_Alexander_Glinz.jpg. [Accessed 21 August 2017].

[2] M. Toscano et al., “Unmanned aircraft systems roadmap to the future,” in *Kansas Unmanned Systems Conference*, Kansas, 2013.

[3] T. de Castella, “Where you can and can't fly a drone,” BBC News Magazine, 9 December 2014. [Online]. Available: http://www.bbc.com/news/magazine-30387107. [Accessed 21 August 2017].

[4] B. Torvik, K. E. Olsen and H. D. Griffithst, “X-band measurements of radar signatures of large sea birds,” in *International Radar Conference*, Lille, France, 2014.

[5] J. Edwards and E. W. Houghton, “Radar echoing area polar diagrams of birds,” *Nature*, vol. 184, pp. 1059-1059, 1959.

[6] C. R. Vaughn, “Birds and insects as radar targets: a review,” *Proceedings of the IEEE*, vol. 73, no. 2, pp. 205-227, 1985.

[7] P. Molchanov et al., “Classification of small UAVs and birds by micro-doppler signatures,” *International Journal of Microwave and Wireless Technologies*, vol. 6, no. 3/4, pp. 435-444, 2014.

[8] B. Torvik, “Investigation of non-cooperative target recognition of small and slow moving air targets in modern air defence surveillance radar,” Ph.D. dissertation, Department of Electrical and Electronic Engineering, University College London, 2016. [Online]. Available: http://discovery.ucl.ac.uk/1532017/. [Accessed 21 August 2017].

[9] J. J. M. de Wit, R. I. A. Harmanny and P. Molchanov, “Radar micro-doppler feature extraction using the singular value decomposition,” in *2014 International Radar Conference*, 2014.

[10] R. I. A. Harmanny, J. J. M. de Wit and G. Premel-Cabic, “Radar micro-doppler mini-UAV classification using spectrograms and cepstrograms,” *International Journal of Microwave and Wireless Technologies*, vol. 7, no. 3/4, pp. 469-477, 2015.

[11] S. Harman, “Characteristics of the radar signature of multi-rotor UAVs,” in *2016 European Radar Conference (EuRAD)*, 2016.

[12] J. J. M. de Wit, R. I. A. Hermanny and G. Prémel Cabic, “Micro-doppler analysis of small UAVs,” in *2012 9th European Radar Conference (EuRAD)*, 2012.

[13] M. Ritchie, F. Fioranelli and H. Griffiths, “Micro-drone RCS analysis,” in *2015 IEEE Radar Conference*, 2015.

[14] P. Dammert, “On a Few Aspects for MicroDoppler and Drones,” Saab Surveillence, Gothenburg, 2016.

[15] Syahlevi, “Drone Parrot,” via Wikimedia Commons, 16 March 2016. [Online]. Available: https://commons.wikimedia.org/wiki/File:81RNYV29HCL._SL1500_(1).jpg. [Accessed 21 August 2017].

[16] DJI technologies, “Phantom 2 Vision+ quadcopter,” via Wikimedia Commons, 2 June 2014. [Online]. Available: https://commons.wikimedia.org/wiki/File:DJI-Phantom2-Vision-plus.png. [Accessed 21 August 2017].

[17] SkylarkCoder, “Picture of the Yuneec Typhoon H Hexacopter,” via Wikimedia Commons, 13 July 2016. [Online]. Available: https://commons.wikimedia.org/wiki/File:Yuneec_Typhoon_H.jpg. [Accessed 21 August 2017].

[18] M. Miwa et al., “Evaluation of quad ducted-fan helicopter,” *International Journal of Intelligent Unmanned Systems*, vol. 1, no. 2, pp. 187-198, 2013.

[19] Joint Air Power Competence Centre, “Strategic Concept of Employment for Unmanned Aircraft Systems in NATO,” 2010.

[20] J. R. Moon, “A survey of bird flight data relevant to radar tracking systems,” in *Radar 2002*, 2002.

[21] R. M. O’Donnell, “Radar Systems Engineering: Lecture 1 Introduction,” IEEE New Hampshire Section, 1 October 2009. [Online]. Available: http://aess.cs.unh.edu/Radar%202010%20PDFs/Radar%202009%20A%20_1%20Introduction.pdf. [Accessed 21 August 2017].

[22] G. T. Ruck et al., Radar Cross Section Handbook Vol. 1, New York, NY: Plenum Press, 1970.

[23] P. Tait, Introduction to Radar Target Recognition, London: The Institution of Engineering and Technology, 2005.

[24] H. L. Thal and R. J. Garzarelli, “Radar cross section map for straight wire,” *IEEE Transactions on Antennas and Propagation*, vol. 20, no. 1, pp. 82-84, 1972.

[25] C. A. Balanis, Advanced Engineering Electromagnetics, New York, NY: John Wiley & Sons, 1989.

[26] J. Jin, The Finite Element Method in Electromagnetics, 2nd ed., New York, NY: John Wiley & Sons, 2002.

[27] A. Taflove and S. C. Hagness, Computational Electrodynamics: the Finite-Difference Time-Domain Method, 2nd ed., Norwood, MA: Artech House, 2000.

[28] V. C. Chen, The Micro-Doppler Effect in Radar, Norwood: Artech House, 2011.

[29] Stratasys, inc., "GrabCAD," [Online]. Available: https://grabcad.com/. [Accessed 21 August 2017].

[30] Professional Plastics, "Electrical properties of plastic materials," [Online]. Available: http://www.professionalplastics.com/professionalplastics/ElectricalPropertiesofPlastics.pdf. [Accessed 21 August 2017].

[31] Z. M. Elimat et al., "Dielectric properties of epoxy/short carbon fiber composites," *Journal of Materials Science,* vol. 45, no. 19, pp. 5196-5203, 2010.

[32] E. J. Riley, E. H. Lenzing and R. M. Narayanan, "Characterization of radar cross section of carbon fiber composite materials," *SPIE 9461, Radar Sensor Technology XIX; and Active and Passive Signatures VI,* vol. 9461, pp. 946103-1–946103-8, 2015.

[33] E. F. Knott, "Dielectric constant of plastic foams," *IEEE Transactions on Antennas and Propagation,* vol. 41, no. 8, pp. 1167-1171, 1993.

A Comparison of VV-polarised calculations

As can be seen in the figure below, there is a significant difference between calculations at 10 GHz where the VV-polarisation RCS calculated in this study is much larger than the original calculations done prior to this study and with the same conditions. The dielectric constant used here is ε_r=3.0. At the same time, calculations at 3 GHz instead show almost identical results where the small deviations are attributed to different versions of HFSS used as the meshing algorithms of the software are constantly improved. It should also be mentioned that the calculated RCS with HH-polarisation at 10 GHz correspond very well to the original computations.

Comparing the VV-polarisation to the HH-polarisation at 10 GHz, the difference at the broadside flash is 10.2 dB for the calculations in this study and 21.4 dB for the previous calculations. This can be compared to the difference predicted by the cylinder approximation which predicts a difference of 6.5 dB at this dielectric constant and frequency which is closer to the newly calculated values. The cylinder RCS model also predicts a more similar radiation pattern when it comes to lobe widths and as can be seen in the figure below, the originally calculated RCS at VV-polarisation changes its pattern rather significantly in comparison to calculated values for HH-polarisation.

A satisfactory explanation as to why this difference is seen at 10 GHz and not at 3 GHz has not been found as the methods of calculations are seemingly identical.

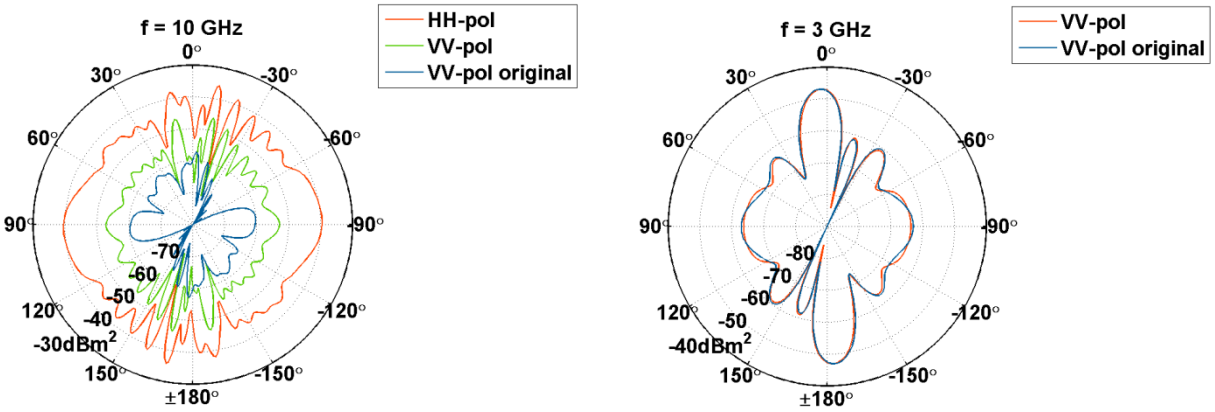

B Details of RCS characteristics

Details of the lobe characteristics of the calculated RCS for different frequencies, dielectric constants and propeller lengths are presented here. Lobes used as broadside flash at each frequency are marked. Decision of which lobe is the broadside flash is based on distinction of lobe, location close to 0° and that amplitude is expected to be higher in relation to other lobes.

RCS of 9x4.7”, sorted by largest RCS for each frequency:

ε_r	Frequency [GHz]	Lobe location [°]	Lobe width [°]	RCS [dBm^2]
2.0	10	10	5	-43.0
		-11	2.9	-43.7
		90	61.5	-51.7
	6	3	7	-39.6
		-6	3.4	-49.2
	3	3	12.5	-45.7
		-17	8	-56.1
	1	20	56.1	-65.5
3.4	10	-11	3.4	-33.6
		-87	36	-35.4
	6	4	7	-31.7
		-6	3.5	-40.8
	3	3	12.6	-38.1
		-17	8.1	-48.1
	1	7	45.6	-57.4
		-88	35.8	-67.5
5.7	10	-86	23.1	-20.6
		4	4.1	-26.0
		-10	3.9	-26.1
	6	4	7	-25.6
		-6	3.6	-34.4
	3	3	12.6	-32.0
		-17	8.2	-41.8
	1	4	40.4	-50.9
		-86	53.4	-63.0
8.0	10	61	12.3	-20.6
		4	4.5	-21.6
		-10	5	-25.1
		35	6.7	-27.0
		90	14.8	-27.1
	6	4	7.1	-22.4
		-6	3.7	-30.7
	3	3	12.7	-28.2
		-17	8.3	-37.9
	1	4	38.7	-47.2
		-84	55.9	-60.3
∞	10	3	3.4	-21.7

		9	4	-23.0
		-4	4.3	-24.4
		-74	10.9	-27.6
	6	1	5.6	-19.0
		-66	14.4	-21.8
		14	5.6	-22.3
		-8	7.5	-23.7
		65	14.1	-26.2
	3	2	10.5	-16.3
		-56	20	-18.6
		58	19.1	-20.4
		-17	8.5	-22.8
	1	3	75.5	-15.5

RCS 10x4.7”, sorted by largest RCS for each frequency:

ε_r	Frequency [GHz]	Lobe location [°]	Lobe width [°]	RCS [dBm^2]
8.0	10	-57	10	-24.8
		19.5	4.1	-25.0
		54	8.3	-25.1
		-1	3.7	-25.2
		-18	5.1	-26.0
		9	3.6	-26.1
		31.5	3.6	-26.6
		89	16.3	-27.0
	6	-1	6.1	-24.3
		-16	8.7	-28.5
		15	5.9	-29.8
	3	-1	10.4	-29.6
		33	11.3	-36.8
		-35	13	-36.8
	1	-2	32.7	-48.6

RCS 11x4.7”, sorted by largest RCS for each frequency:

ε_r	Frequency [GHz]	Lobe location [°]	Lobe width [°]	RCS [dBm^2]
8.0	10	75.5	14	-18.9
		11	3.6	-21.7
		-13	3.3	-22.2
		50	6.5	-24.9
		-4	11.3	-28.0
	6	14	12.5	-24.9
		-15	4.2	-28.5
	3	5	10.3	-26.4
		-12	7.3	-32.5
		-26	6.8	-40.6
	1	6	30.4	-44.0

C Duct with propeller

Calculations of a propeller inside a duct at f=10 GHz with ε_r=8.0 and ε_r=1.03 which could correspond roughly to carbon fibre which is highly reflective and Styrofoam which is highly transparent. The dielectric constant of the propeller is in both cases ε_r=8.0. It is seen that the calculations with only the duct and the calculations with the propeller and duct are almost identical for the higher dielectric constant where the propeller is hardly hidden for the case with lower dielectric constant. A comparison is shown with the RCS from the propeller only. Moreover, the complex-valued electric fields of the calculations of duct with propeller and only the duct are subtracted from each other as this would result in something close to the propeller RCS. In the case of high dielectric constant, it is seen that the subtracted fields correspond somewhat to the propeller RCS, mostly at or near end-fire, whereas in the case of low dielectric constant the subtracted fields are nearly identical to the propeller RCS. This shows the large impact of the high dielectric constant duct on the overall RCS as wave phenomena such as dampening effects or multiple reflections distorts the propeller RCS.

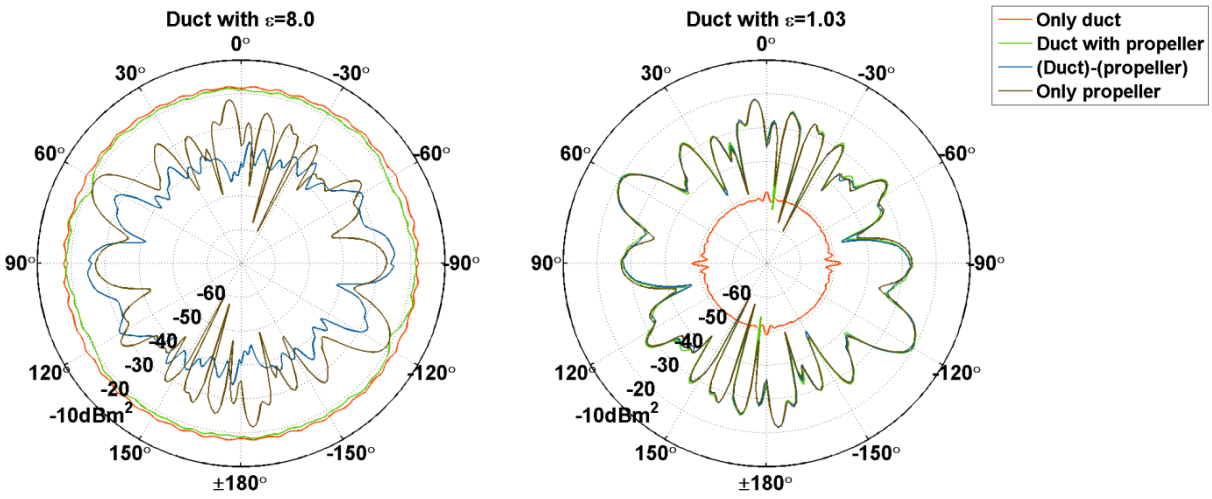

D Matlab script for calculating micro-Doppler signatures

The Matlab script used for generating the micro-Doppler signature. Matlab 2013b was used which does not include any function for creating polar plots. The function *mmpolar(...)* was downloaded from an online open source database to accomplish this.

```
%% micro-Doppler signature of multiple propellers
clc
clear all;

%%%%%%%%%%%%%%%%%%%%%%%%%%%%%%%%%%%%%%%%%%%%%%%
% Import data into RCSPhi and phi variables
%%%%%%%%%%%%%%%%%%%%%%%%%%%%%%%%%%%%%%%%%%%%%%%
data=csvread('./data_HFSS_RCS_v18/RCS_9x4,7/Nylon/rcs_prop_9x4,7_10GHz_eps_
3,4_pol_hh.csv',1,0);
f0 = 10e9;  % radar frequency for calculations [Hz]
r = (9*0.0254) / 2; % radius of propeller [m]

RCSPhi_ccw = data(:,2) + data(:,3)*1i;
RCSPhi_ccw= [RCSPhi_ccw(1:end-1); RCSPhi_ccw(1:end)];
phi = data(:,1);
phi = ([phi(1:end-1); 180+phi(1:end)])*pi/180;

RCSPhi_cw = flipud(RCSPhi_ccw); % Create RCS for CW blade


% Plot RCS
figure(1)
subplot(1,2,1)
mmpolar(phi,20*log10(abs(RCSPhi_cw)),'b')
mmpolar('TZeroDirection','north','RLimit',[-55 -15],'TTickDelta',30)
title('RCS CW')
subplot(1,2,2)
mmpolar(phi,20*log10(abs(RCSPhi_ccw)),'b')
mmpolar('TZeroDirection','north','RLimit',[-55 -15],'TTickDelta',30)
title('RCS CCW')



%%%%%%%%%%%%%%%%%%%%%%%%%%%%%%%%%%%%%%%%%%%%%%%
% Sample time signal
%%%%%%%%%%%%%%%%%%%%%%%%%%%%%%%%%%%%%%%%%%%%%%%
% Parameters and constants
n_prop = 1    % no. of propellers
T_end = 20e-3;  % signal length [s]
Fs = 15000;     % sample rate (PRF) [Hz]

N = floor(Fs*T_end);        % no. of samples
dt = 1/Fs;                  % timestep
t = linspace(dt,T_end,N);
c0 = 299792458;


% Initiate vectors
omega = zeros(n_prop,1);
phi_rot_start = zeros(n_prop,1);
f_tip = zeros(n_prop,1);
v_tip = zeros(n_prop,1);
Y = zeros(N,1);
```

```
% Setup propeller parameters
% omega(#) is the rotation speed of propeller #, RPS*(2*pi). [rad/s]
% phi_rot_start(#) is the rotation start phase of propeller #. [rad]
omega(1) = -125*2*pi;
phi_rot_start(1) = 90*pi/180;

omega(2) = 137.16*2*pi;
phi_rot_start(2) = 15*pi/180;

omega(3) = -112.2*2*pi;
phi_rot_start(3) = -43*pi/180;

omega(4) = 126.27*2*pi;
phi_rot_start(4) = 151*pi/180;

omega(5) = -116.3*2*pi;
phi_rot_start(5) = 83*pi/180;

omega(6) = 134.52*2*pi;
phi_rot_start(6) = 39*pi/180;

omega(7) = -122.46*2*pi;
phi_rot_start(7) = -13*pi/180;

omega(8) = 129.33*2*pi;
phi_rot_start(8) = 103*pi/180;


for k = 1:n_prop
    v_tip(k) = abs(r*omega(k));
    f_tip(k) = abs(2*v_tip(k) / c0 * f0 / 1000);

    fprintf('Rotor %i\n',k)
    fprintf('RPS: %.3f\n',omega(k)/(2*pi))
    fprintf('Speed of tip: %.3f m/s\n', v_tip(k))
    fprintf('Doppler shift of tip: %.3f kHz\n', f_tip(k))
    fprintf('\n')
end
fprintf('Mean rotor RPS: %.3f\n\n',mean(abs(omega(1:n_prop)/2/pi)))


% Sample the signal in time
for k = 1:N
    for m = 1:n_prop
        temp_phi = k*dt*omega(m) + phi_rot_start(m);
        temp_phi = mod(temp_phi-phi(1), 2*pi)+phi(1);
        temp_phi = floor(temp_phi*1e4)/1e4; % round to 4 decimals

        if omega(m) > 0
            Y(k) = Y(k) + RCSPhi_cw(find(phi>=temp_phi,1));
        else
            Y(k) = Y(k) + RCSPhi_ccw(find(phi>=temp_phi,1));
        end
    end
end


% Generate STFT for joint time-frequency representation
% n_size = N     % Use to specify sample size in no. of samples (use N for
long integration time)
```

```
n_size = floor(2e-3/dt) % Use to specify sample size in time (1 or 2 ms
seems good)
overlap = 0.9;
[s,fsp,tsp] = spectrogram(Y,hamming(n_size),floor(overlap*n_size),Fs,Fs);
fsp = linspace(-Fs/2,Fs/2,length(fsp));



%%%%%%%%%%%%%%%%%%%%%%%%%%%%%%%%%%%%%%%%%%%%%%%%
% Plot results
%%%%%%%%%%%%%%%%%%%%%%%%%%%%%%%%%%%%%%%%%%%%%%%%
% Plot time signal
figure(2)
plot(t/1e-3,abs(Y),'b'), grid on
xlabel('Time [ms]')
ylabel('Amplitude')

% Plot m-D spectrum
figure(3)
imagesc(tsp/1e-3,fsp/1e3,20*log10(abs(fftshift(s,1))))
xlabel('Time [ms]')
ylabel('Frequency [kHz]')

set(gca,'YDir','normal') % flip data to get increasing values of f upwards
h = colorbar;
colormap 'jet'
ylabels = get(h,'YTickLabel');
unit = ' ' * ones(length(ylabels),3);
unit(end,1:3) = ' dB';
set(h,'YTickLabel',strcat(ylabels, unit));
```